

Article

# A Dual-Voltage-Vector Model-Free Predictive Current Controller for Synchronous Reluctance Motor Drive Systems

Cheng-Kai Lin <sup>1,\*</sup> , Jen-te Yu <sup>2</sup>, Hao-Qun Huang <sup>1</sup>, Jyun-Ting Wang <sup>1</sup>, Hsing-Cheng Yu <sup>3</sup> and Yen-Shin Lai <sup>4</sup>

<sup>1</sup> Department of Electrical Engineering, National Taiwan Ocean University, Keelung 202, Taiwan; hacha4139@gmail.com (H.-Q.H.); smile19950625@gmail.com (J.-T.W.)

<sup>2</sup> Department of Electrical Engineering, Chung Yuan Christian University, Taoyuan 320, Taiwan; yu@cycu.edu.tw

<sup>3</sup> Department of Systems Engineering and Naval Architecture, National Taiwan Ocean University, Keelung 202, Taiwan; hcyu@ntou.edu.tw

<sup>4</sup> Department of Electrical Engineering, National Taipei University of Technology, Taipei 106, Taiwan; yslai@ntut.edu.tw

\* Correspondence: cklin@mail.ntou.edu.tw; Tel.: +886-2-2462-2192 (ext. 6231)

Received: 28 May 2018; Accepted: 29 June 2018; Published: 3 July 2018



**Abstract:** For current control in power conversion and motor drive systems, there exist three classic methods in the literature and they are the hysteresis current control (HCC), the sine pulse-width modulation (SPWM), and the space vector pulse width modulation (SVPWM). HCC is easy to implement, but has relatively large current harmonic distortion as the disadvantage. On the other hand, the SPWM and SVPWM use modulation technique, commonly together with at least one proportional-integral (PI) regulator to reduce load current ripples, and hence demanding more computation time. This paper aims to improve the performance of a recently proposed new current control method—the single-voltage-vector model predictive current control (SVV-MPCC), for synchronous reluctance motor (SynRMs) drives. To that end, a dual-voltage-vector model-free predictive current control (DVV-MFPCC) for SynRMs is proposed. Unlike the SVV-MPCC that applies only a single voltage vector per sampling period, the proposed DVV-MFPCC is capable of providing two successive segmentary current predictions in the next sampling period through all possible combinations from any two candidate switching states increasing the number of applicable switching modes from seven to nineteen and reducing the prediction error effectively. Moreover, the new control does not utilize any parameters of the SynRM nor its mathematical model. The performance is effectively enhanced compared to that of SVV-MPCC. The working principle of the DVV-MFPCC will be detailed in this paper. Finally, the SVV-MPCC, the single-voltage-vector model-free predictive current control (SVV-MFPCC), the dual-voltage-vector model predictive current control (DVV-MPCC), and the DVV-MFPCC are realized to control the stator currents of SynRM through a 32-bit microcontroller TMS320F28377S. Experimental results are provided to validate the new method and verify that the DVV-MFPCC performs better than do the SVV-MPCC, the SVV-MFPCC, and the DVV-MPCC.

**Keywords:** predictive current control; synchronous reluctance motor; voltage source inverter

## 1. Introduction

With an appropriate device [1], fuel energy can be converted into mechanical/kinetic energy. In comparison to that process, electric motors are used to convert electrical energy into

mechanical/kinetic energy. Among various motor types, the synchronous reluctance motors (SynRMs) have been widely used in washing machines, air conditioners, and electric vehicles thanks to their robustness, simple structure, and without use of magnetic materials. In order to achieve high performance so as to save energy/power under different operation conditions, many current control methods have been developed in the past, such as hysteresis current control [2], pulse width modulation (PWM) [3], space vector PWM (SVPWM) [4], and model predictive current control (MPCC) [5,6]. The first two methods, as limited by their nature, cannot predict future current in next sampling period. To date, a lot of research results in predictive current controllers have been reported and applied to motor drive systems and other applications. In addition to the MPCC, other model predictive control techniques and related applications are thriving as well. For example, a predictive control was applied to renewable energy systems [7]. Nauyen and Kim [8] proposed a modulated finite control set-model predictive control scheme for a grid-connected inverter under distorted grid conditions. Yang et al. [9] proposed a predictive power control strategy for doubly fed induction generators (DFIGs) based on a wind energy converter system. Jin et al. [10] presented a model predictive direct power control for nonredundant fault tolerant grid-connected bidirectional voltage source converter (BVSC). The proposed method was investigated for continuous operation in that paper, even if the BVSC has leg open-circuits faults. Guzmán et al. proposed a finite control set model predictive control for a three-phase shunt active power filter with a Kalman filter-based estimation [11]. Using their method, the grid currents can be successfully controlled. In [12], a model-based predictive current control (MBPCC) method with constant switching frequency was used to control the load current of a single-phase voltage source inverter. This method can generate switching patterns with a constant switching frequency while maintaining the fast dynamics of traditional predictive current control. An improved continuous-time model predictive control for permanent magnetic synchronous motors was proposed in [13] to achieve a wide-speed range operation. A near state vector selection-based model predictive control (NSV-MPC) scheme was presented by Dadu et al. [14] to mitigate the common mode voltage of a three-phase four-leg inverter and reduce the computational burden. In [15], the model predictive control was applied to induction machines. In [16], an improved finite-control-set model predictive control with reduced computational complexity and fast dynamic response was presented for cascaded H-bridge inverters. In [17], a finite set-model predictive control successfully controlled the load current of a three voltage source inverter via a development field-programmable gate array (FPGA) kit. Espi and Castillo [18] studied a new integral predictive current control in LCL-filtered grid-connected converters to mitigate grid current distortion.

Among these existing methods, the model predictive current control (MPCC) [6] is a very important one whose control principle is based on discrete mathematical model of the system under control. This approach, however, suffers from two major shortcomings: the back EMF estimation errors and the system parameter uncertainties and variations, which lead to its unsatisfactory current prediction performance. In addition, the MPCC is suitable for decoupled systems, but not so for coupled ones resulting in a technical bottleneck for the back EMF estimation.

The single-voltage-vector model-free predictive current control (SVV-MFPCC) [19–23] has recently received some attention, as it does not rely on system's mathematical models and parameters, nor on the back EMFs. As such, the SVV-MFPCC exhibits better current-tracking performance thanks to its lesser sensitivity to parameter variations. Existing SVV-MFPCC only applies one out of seven candidate voltage vectors in each sampling period, including six active-voltage vectors and one zero-voltage vector. To enhance the performance of current prediction, this paper proposes a dual-voltage-vector MFPCC (DVV-MFPCC) that applies two switching states rather than one in each sampling period. Through linear combination, the number of candidate voltage vectors is increased from the original seven to nineteen, meaning that a lot of extra states can be utilized. The stator current will be detected twice in each sampling period, with each detection interval halves the sampling period. Although the method in [23] worked well under a three-phase resistive-inductive (RL) load, its success on the SynRM drive system cannot be guaranteed without further confirmation from experimental

results. Comparatively (in the hardware sense), an older digital signal processor (DSP) TMS320F28335 was used in [23], yet a newer microcontroller is used in current study for performing experiments to support and validate the proposed DVV-MFPCC. The differences between these two methods for current prediction are summarized in Table 4. As for the experimental results, there were only 4 waveforms in [23] lacking quantitative data. In contrast to that, this paper provides 60 waveforms as well as quantitative data.

It can be observed from [24,25] that one of the future research trends is to split one sampling period into multiple equal intervals to generate more selectable switching modes enabling discrete space vector modulation (DSVM) to predict three switching states in the next sampling period, which is a great advantage. It is worth noting that [24,25] are model-based approaches. Yet to this day there is, to the authors' best knowledge, no literature reports result that combines MFPCC [22] with DSVM [24,25] for SynRM drive systems. Toward that end, more new technology and hardware breakthroughs obviously will have to be further advanced and realized. Motivated by its future potential and to push forward innovative control methods and technologies, a preparatory study is therefore very much needed leading to this work.

Finally, the proposed DVV-MFPCC is implemented via the microcontroller TMS320F28377S and applied to a synchronous reluctance motor (SynRM) drive system for validation and feasibility verification.

The rest of this paper is organized as follows: single-voltage-vector model and model-free predictive current controls are introduced in Sections 2 and 3, respectively. The dual-voltage-vector model and model-free methods are detailed in Sections 4 and 5, respectively. Section 6 gives experimental data and results to verify the feasibility of the proposed method and validate the salience in terms of its performance. Finally, Section 7 provides the conclusion.

## 2. Single-Voltage-Vector Model Predictive Current Control (SVV-MPCC)

Figure 1 shows a six-switch three-phase inverter connected to a SynRM, where  $V_{dc}$  is the DC link voltage;  $L_{aa}$ ,  $L_{bb}$ , and  $L_{cc}$  are three-phase self-inductances;  $e_a$ ,  $e_b$ , and  $e_c$  are three-phase back EMFs; and  $S_{a1}$ ,  $S_{a0}$ ,  $S_{b1}$ ,  $S_{b0}$ ,  $S_{c1}$ ,  $S_{c0}$  are the six power switches of the inverter. This SynRM drive system has seven switching states, denoted as  $S_0, S_1, \dots, S_6$ , and their corresponding seven voltage vectors  $V_0, V_1, \dots, V_6$ . Figure 2 illustrates the seven voltage vectors.

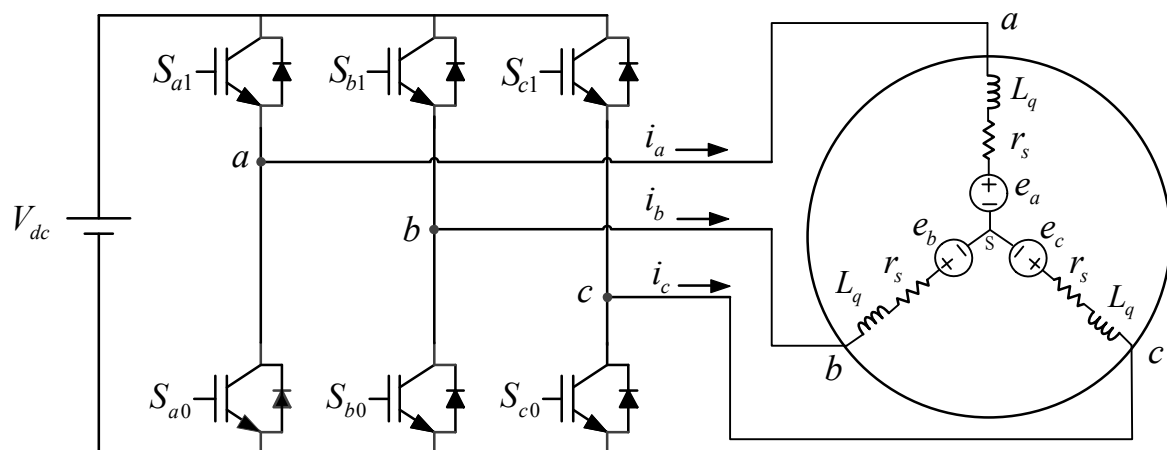


Figure 1. Six-switch three-phase inverter connected to a SynRM.

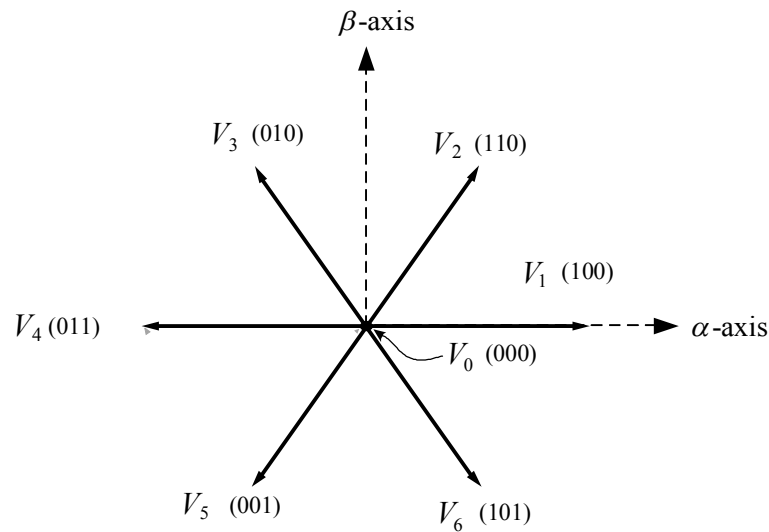


Figure 2. Seven voltage vectors.

The equivalent stator voltage equations of the SynRM on the  $\alpha$ - $\beta$  axes can be written as:

$$v_\alpha = r_s i_\alpha + L_q \frac{di_\alpha}{dt} + E_\alpha \quad (1)$$

$$v_\beta = r_s i_\beta + L_q \frac{di_\beta}{dt} + E_\beta \quad (2)$$

where  $i_\alpha$  and  $i_\beta$  are stator currents;  $v_\alpha$  and  $v_\beta$  are stator voltages;  $E_\alpha$  and  $E_\beta$  represent extended back EMFs [22];  $L_q$  is the  $q$ -axis inductance;  $r_s$  denotes the stator resistance, and  $d/dt$  is the differential operator.

Expressed in discrete-time forms, Equations (1) and (2) can be rewritten as:

$$v_{\alpha,\beta}(k) = r_s i_{\alpha,\beta}(k) + L_q \frac{i_{\alpha,\beta}(k) - i_{\alpha,\beta}(k-1)}{T_s} + E_{\alpha,\beta}(k) \quad (3)$$

where  $T_s$  is the sampling period, and  $k$  stands for the ( $k$ )th sampling. Following Equation (3) with some manipulations, one can get the  $k$ th and ( $k+1$ )th stator currents as follows:

$$i_{\alpha,\beta}(k) = \frac{L_s i_{\alpha,\beta}(k-1) + T_s v_{\alpha,\beta}(k) - T_s E_{\alpha,\beta}(k)}{r_s T_s + L_q} \quad (4)$$

$$i_{\alpha,\beta}(k+1) = \frac{L_s i_{\alpha,\beta}(k) + T_s v_{\alpha,\beta}(k+1) - T_s E_{\alpha,\beta}(k+1)}{r_s T_s + L_q} \quad (5)$$

The  $k$ th back EMF can be estimated by

$$\hat{E}_{\alpha,\beta}(k) = v_{\alpha,\beta}(k) + \frac{L_q}{T_s} i_{\alpha,\beta}(k-1) - \frac{r_s T_s + L_q}{T_s} i_{\alpha,\beta}(k) \quad (6)$$

where the hat “ $\hat{\phantom{x}}$ ” refers to the estimated counterpart. Assume the sampling period is short enough, the ( $k+2$ )th back EMF can be approximated by the  $k$ th estimated value, i.e.,

$$E_{\alpha,\beta}(k+2) \approx \hat{E}_{\alpha,\beta}(k) \quad (7)$$

According to Equations (4)–(7), the prediction of the ( $k+2$ )th sampled current under the switching state  $S_i$  can be calculated by

$$i_{\alpha,\beta}^p(k+2)|_{S_i} = \frac{L_s i_{\alpha,\beta}(k+1) + T_s v_{\alpha,\beta}(k+2)|_{S_i} - T_s \hat{E}_{\alpha,\beta}(k)}{r_s T_s + L_q} \quad (8)$$

where the superscript “*p*” denotes prediction, and  $S_i$  belongs to  $\{S_0, \dots, S_6\}$ . Next, a cost function is defined as

$$g|_{S_i} = \left| i_{\alpha}^*(k) - i_{\alpha}^p(k+2)|_{S_i} \right| + \left| i_{\beta}^*(k) - i_{\beta}^p(k+2)|_{S_i} \right| \quad (9)$$

where the superscript “\*” represents the reference value. The switching criterion is set as selection of the state  $S_g$  that yields the minimum cost value, that is

$$g|_{S_g \in \{S_0, \dots, S_6\}} = \min \left\{ g|_{S_0}, \dots, g|_{S_6} \right\} \quad (10)$$

The switching status  $S_g$  will be outputted to the inverter in the next sampling period completing the MPCC design. More details can be found in [22].

### 3. Single-Voltage-Vector Model-Free Predictive Current Control (SVV-MFPCC)

During the application of the  $(k-1)$ th,  $(k)$ th, and  $(k+1)$ th switching states, designated as  $S_{k-1}$ ,  $S_k$ , and  $S_{k+1}$ , the corresponding current differences can be calculated by the following equations:

$$\Delta i_{\alpha,\beta}|_{S_{k-1}} = i_{\alpha,\beta}(k)|_{S_{k-1}} - i_{\alpha,\beta}(k-1)|_{S_{k-2}} \quad (11)$$

$$\Delta i_{\alpha,\beta}|_{S_k} = i_{\alpha,\beta}(k+1)|_{S_k} - i_{\alpha,\beta}(k)|_{S_{k-1}} \quad (12)$$

$$\Delta i_{\alpha,\beta}|_{S_{k+1}} = i_{\alpha,\beta}(k+2)|_{S_{k+1}} - i_{\alpha,\beta}(k+1)|_{S_k} \quad (13)$$

Based on Equations (12) and (13), the  $(k+2)$ th sampled current under the switching state  $S_j$  can be expressed as

$$i_{\alpha,\beta}(k+2)|_{S_j} = i_{\alpha,\beta}(k)|_{S_{k-1}} + \Delta i_{\alpha,\beta}|_{S_k} + \Delta i_{\alpha,\beta}|_{S_j=S_{k+1}} \quad (14)$$

Assume that the sampling frequency is high enough, the stator current difference can be replaced by its previous value under the same switching state, i.e.,

$$\Delta i_{\alpha,\beta}|_{S_k} \approx \Delta i_{\alpha,\beta,pre}|_{S_i=S_k}, i \in \{0, \dots, 6\} \quad (15)$$

$$\Delta i_{\alpha,\beta}|_{S_{k+1}} \approx \Delta i_{\alpha,\beta,pre}|_{S_j=S_{k+1}}, j \in \{0, \dots, 6\} \quad (16)$$

where the subscript “*pre*” denotes previous value. Using Equations (15) and (16), one can calculate the predicted current of Equation (14) via

$$i_{\alpha,\beta}^p(k+2)|_{S_j} = i_{\alpha,\beta}(k)|_{S_k} + \Delta i_{\alpha,\beta,pre}|_{S_k} + \Delta i_{\alpha,\beta,pre}|_{S_j=S_{k+1}} \quad (17)$$

Based on Equation (17), one can get seven cost values under the seven switching states. The switching state yielding minimum cost value will then be applied to the inverter in the next sampling period. More details can be found in [22].

### 4. Dual-Voltage-Vector Model Predictive Current Control (DVV-MPCC)

After synthesis of the dual voltage vectors, 19 switching modes, denoted as  $Q_0, \dots, Q_{18}$ , will become applicable to the inverter whose corresponding synthesized voltage vectors are listed in Table 1 and shown in Figure 3. Since the number of switching mode is increased to 19, the Equations (8)–(10) should be modified as follows:

$$i_{\alpha,\beta}^p(k+2) \Big|_{Q_i \in \{Q_0, \dots, Q_{18}\}} = \frac{L_s i_{\alpha,\beta}(k+1) + T_s v_{\alpha,\beta}(k+2) \Big|_{Q_i} - T_s \hat{E}_{\alpha,\beta}(k)}{r_s T_s + L_q} \quad (18)$$

$$g \Big|_{Q_i} = \left| i_{\alpha}^*(k) - i_{\alpha}^p(k+2) \Big|_{Q_i} \right| + \left| i_{\beta}^*(k) - i_{\beta}^p(k+2) \Big|_{Q_i} \right| \quad (19)$$

$$g \Big|_{Q_g \in \{Q_0, \dots, Q_{18}\}} = \min \left\{ g \Big|_{Q_0}, \dots, g \Big|_{Q_{18}} \right\} \quad (20)$$

Following the prediction principle of the MPCC stated above, the switching mode  $Q_g$  will be applied to control the inverter in the next sampling period completing the DVV-MPCC design.

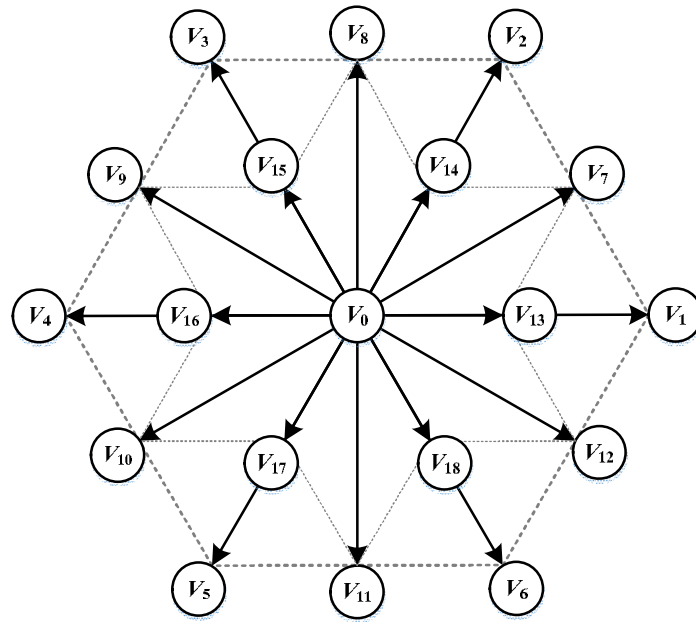


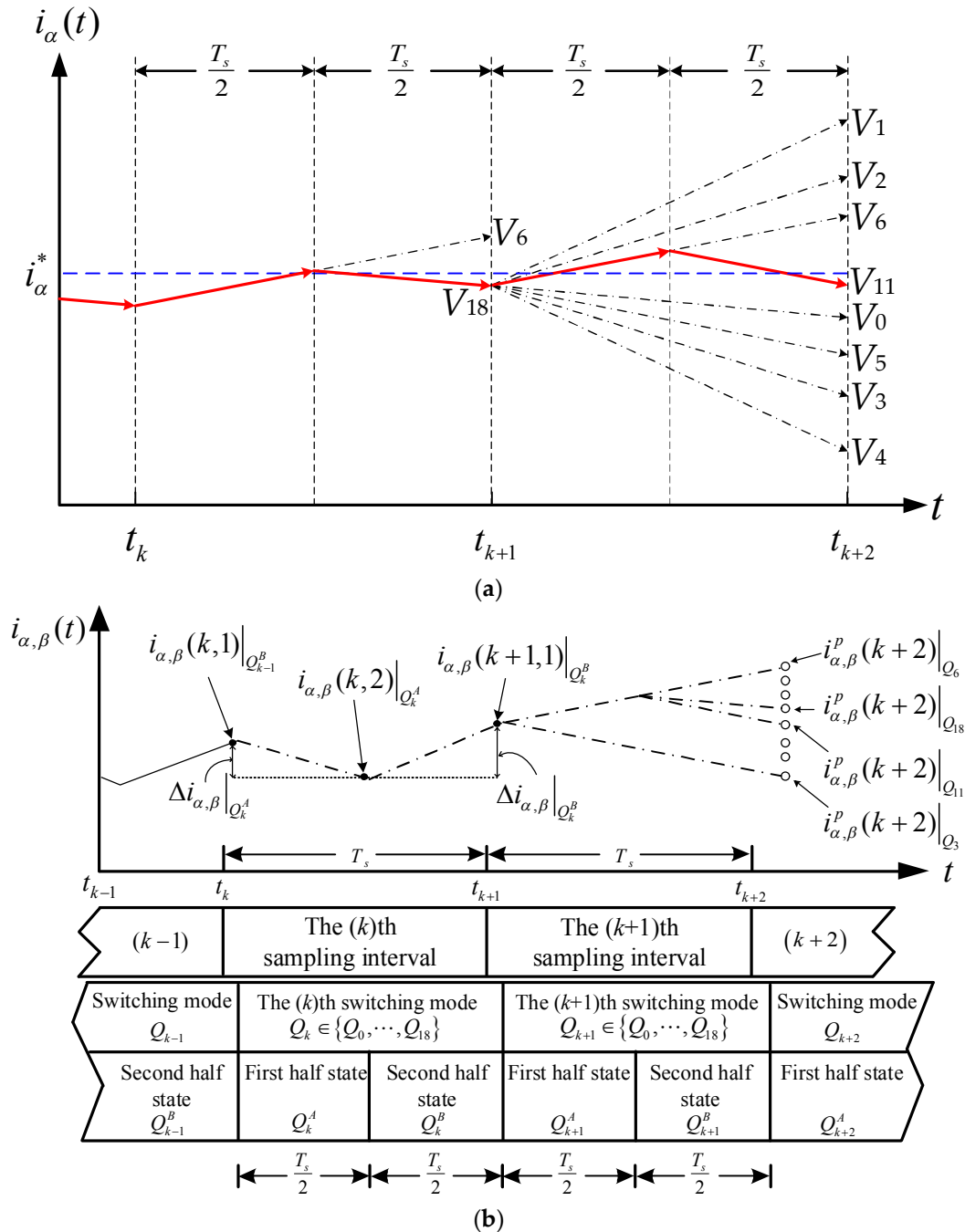
Figure 3. Nineteen synthesized voltage vectors.

Table 1. Correspondence between switching modes and the synthesized vectors.

Switching Mode	Switching States Represented by Switching Functions		Synthesized Voltage Vector
	First $T_s/2$	Second $T_s/2$	
$Q_0$	(000)	(000)	$V_0 = V_0/2 + V_0/2$
$Q_1$	(100)	(100)	$V_1 = V_1/2 + V_1/2$
$Q_2$	(110)	(110)	$V_2 = V_2/2 + V_2/2$
$Q_3$	(010)	(010)	$V_3 = V_3/2 + V_3/2$
$Q_4$	(011)	(011)	$V_4 = V_4/2 + V_4/2$
$Q_5$	(001)	(001)	$V_5 = V_5/2 + V_5/2$
$Q_6$	(101)	(101)	$V_6 = V_6/2 + V_6/2$
$Q_7$	(100)	(110)	$V_7 = V_1/2 + V_2/2$
$Q_8$	(110)	(010)	$V_8 = V_2/2 + V_3/2$
$Q_9$	(010)	(011)	$V_9 = V_3/2 + V_4/2$
$Q_{10}$	(011)	(001)	$V_{10} = V_4/2 + V_5/2$
$Q_{11}$	(001)	(101)	$V_{11} = V_5/2 + V_6/2$
$Q_{12}$	(101)	(100)	$V_{12} = V_6/2 + V_1/2$
$Q_{13}$	(100)	(000)	$V_{13} = V_1/2 + V_0/2$
$Q_{14}$	(110)	(000)	$V_{14} = V_2/2 + V_0/2$
$Q_{15}$	(010)	(000)	$V_{15} = V_3/2 + V_0/2$
$Q_{16}$	(011)	(000)	$V_{16} = V_4/2 + V_0/2$
$Q_{17}$	(001)	(000)	$V_{17} = V_5/2 + V_0/2$
$Q_{18}$	(101)	(000)	$V_{18} = V_6/2 + V_0/2$

### 5. Dual-Voltage-Vector Model-Free Predictive Current Control (DVV-MFPCC)

Seemingly the proposed DVV-MFPCC with a sampling period of 100 microseconds is equivalent to the SVV-MFPCC with a sampling period of 50 microseconds. Technically, however, there exists significant differences between the two concepts. Unlike SVV-MFPCC, the proposed DVV-MFPCC is capable of providing two successive segmentary current predictions in the next sampling period through all possible combinations from any two candidate switching states, as depicted by Figure 4a.



**Figure 4.** The features of dual-voltage-vector model-free predictive current control (DVV-MFPCC), including: (a) conceptual comparison of current prediction for the single-voltage-vector model-free predictive current control (SVV-MFPCC) [22] (black dashed line) and the proposed DVV-MFPCC (red solid line); (b) two current samples and two applied switching states during one sampling interval.

The SVV-MFPCC [22] applies one voltage vector during a sampling period, whereas the proposed DVV-MFPCC produces 18 active vectors and a zero vector as listed in Table 1. The conceptual comparison of current prediction is shown in Figure 4a in which the synthesized voltage vectors  $V_0, V_1, V_2, V_3, V_4, V_5, V_6,$  and  $V_{11}$  are candidate vectors. At the time instant  $t_{k+1}$ , it can be observed that the error between the current command  $i_\alpha^*$  (blue dashed line) and the stator current produced by  $V_{18}$  is smaller than that of  $V_6$ . Similarly, at time instant  $t_{k+1}$ , the current ripple produced by the synthesized voltage vector  $V_{11}$  is minimum. As an illustration, Figure 4a clearly shows that the proposed DVV-MFPCC has a smaller current error than does the existing SVV-MFPCC [22] due to the extra available synthesized voltage vectors.

Figure 4b shows current predictions of the DVV-MFPCC, where  $Q_{k-1}, Q_k, Q_{k+1},$  and  $Q_{k+2} \in \{Q_0, \dots, Q_{18}\}; Q_{k-1}^B, Q_k^A, Q_k^B, Q_{k+1}^A, Q_{k+1}^B,$  and  $Q_{k+2}^A \in \{(000), \dots, (111)\}; i_{\alpha,\beta}(k,1)|_{Q_{k-1}^B}$  means that the first current detection will be conducted before the end of the applied switching state  $Q_{k-1}^B$  in the  $k$ th sampling interval;  $i_{\alpha,\beta}(k,2)|_{Q_k^A}$  means that the second current detection will be performed before the end of the applied switching state  $Q_k^A$ . The time interval for each of which is half of the sampling period. During the applications of switching states  $Q_k^A, Q_k^B, Q_{k+1}^A,$  and  $Q_{k+1}^B,$  their corresponding current differences are defined as follows:

$$\Delta i_{\alpha,\beta}|_{Q_k^A} = i_{\alpha,\beta}(k,2)|_{Q_k^A} - i_{\alpha,\beta}(k,1)|_{Q_{k-1}^B} \quad (21)$$

$$\Delta i_{\alpha,\beta}|_{Q_k^B} = i_{\alpha,\beta}(k+1,1)|_{Q_k^B} - i_{\alpha,\beta}(k,2)|_{Q_k^A} \quad (22)$$

$$\Delta i_{\alpha,\beta}|_{Q_{k+1}^A} = i_{\alpha,\beta}(k+1,2)|_{Q_{k+1}^A} - i_{\alpha,\beta}(k+1,1)|_{Q_k^B} \quad (23)$$

$$\Delta i_{\alpha,\beta}|_{Q_{k+1}^B} = i_{\alpha,\beta}(k+2,1)|_{Q_{k+1}^B} - i_{\alpha,\beta}(k+1,2)|_{Q_{k+1}^A} \quad (24)$$

Given Equation (17), one can obtain the following Equations from Equations (21)–(24)

$$i_{\alpha,\beta}(k+1,1)|_{Q_k^B} = i_{\alpha,\beta}(k,1)|_{Q_{k-1}^B} + \Delta i_{\alpha,\beta}|_{Q_k^A} + \Delta i_{\alpha,\beta}|_{Q_k^B} \quad (25)$$

$$i_{\alpha,\beta}(k+2,1)|_{Q_{k+1}^B} = i_{\alpha,\beta}(k+1,1)|_{Q_k^B} + \Delta i_{\alpha,\beta}|_{Q_{k+1}^A} + \Delta i_{\alpha,\beta}|_{Q_{k+1}^B} \quad (26)$$

Substitution of Equation (25) into (26) leads to

$$i_{\alpha,\beta}(k+2,1)|_{Q_{k+1}^B} = i_{\alpha,\beta}(k,1)|_{Q_{k-1}^B} + \Delta i_{\alpha,\beta}|_{Q_k^A} + \Delta i_{\alpha,\beta}|_{Q_k^B} + \Delta i_{\alpha,\beta}|_{Q_{k+1}^A} + \Delta i_{\alpha,\beta}|_{Q_{k+1}^B} \quad (27)$$

Similar to Equations (15) and (16), the current differences  $\Delta i_{\alpha,\beta}|_{Q_k^A}, \Delta i_{\alpha,\beta}|_{Q_k^B}, \Delta i_{\alpha,\beta}|_{Q_{k+1}^A},$  and  $\Delta i_{\alpha,\beta}|_{Q_{k+1}^B}$  can be estimated by their previous values. As a result, the prediction of Equation (27) can be expressed as

$$i_{\alpha,\beta}^P(k+2)|_{Q_{k+1} \in \{Q_0, \dots, Q_{18}\}} = i_{\alpha,\beta}(k,1)|_{Q_{k-1}^B} + \Delta i_{\alpha,\beta,pre}|_{Q_k^A} + \Delta i_{\alpha,\beta,pre}|_{Q_k^B} + \Delta i_{\alpha,\beta,pre}|_{Q_{k+1}^A} + \Delta i_{\alpha,\beta,pre}|_{Q_{k+1}^B} \quad (28)$$

where the superscript “P” stands for prediction. A cost function associated with the switching mode  $Q_i$  is defined as

$$G|_{Q_i} = \left| i_\alpha^*(k) - i_\alpha^P(k+2)|_{Q_i} \right| + \left| i_\beta^*(k) - i_\beta^P(k+2)|_{Q_i} \right| \quad (29)$$

where  $Q_i \in \{Q_0, \dots, Q_{18}\}$ . Based on Equation (29), nineteen cost function values can be obtained. Then, a switching mode  $Q_g$  rendering the minimum cost will be selected according to

$$G|_{Q_g \in \{Q_0, \dots, Q_{18}\}} = \min \{ G|_{Q_0}, G|_{Q_1}, \dots, G|_{Q_{18}} \} \quad (30)$$

Finally, the selected switching mode  $Q_g$  comprising of two switching states, listed in Table 1, will be passed to control the six power switches of the inverter (ON or OFF) in the next sampling period. As such, two switching states will be applied for  $T_s/2$  sequentially. To further facilitate exposition of the DVV-MFPCC, its implementation procedure is outlined as follows:

- Step 1: Sample the stator current for the first time, i.e.,  $i_{\alpha,\beta}(k,1)|_{Q_{k-1}^B}$ .
- Step 2: Calculate current difference and update its value, i.e.,  $\Delta i_{\alpha,\beta,pre}|_{Q_{k-1}^B} = i_{\alpha,\beta}(k,1)|_{Q_{k-1}^B} - i_{\alpha,\beta}(k-1,2)|_{Q_{k-1}^A}$ .
- Step 3: Apply the first switching state  $Q_k^A$  for  $T_s/2$  based on the last selected switching mode  $Q_g$ .
- Step 4: Sample the stator current for the second time, i.e.,  $i_{\alpha,\beta}(k,2)|_{Q_k^A}$ .
- Step 5: Calculate the current difference and update its value, i.e.,  $\Delta i_{\alpha,\beta,pre}|_{Q_k^A} = i_{\alpha,\beta}(k,2)|_{Q_k^A} - i_{\alpha,\beta}(k,1)|_{Q_{k-1}^B}$ .
- Step 6: Apply the second switching state  $Q_k^B$  for  $T_s/2$ .
- Step 7: Convert the first sampled stator current from the  $a$ - $b$ - $c$  axes to the  $\alpha$ - $\beta$  axes.
- Step 8: Calculate the  $\alpha$ -axis and  $\beta$ -axis current commands.
- Step 9: Use Equation (28) to get the predicted current value.
- Step 10: Use Equation (29) to obtain the 19 cost function values under the 19 switching modes from  $Q_0$  to  $Q_{18}$ .
- Step 11: Use Equation (30) to find the minimum value and the associated switching mode  $Q_g$ .
- Step 12: Use Table 1 and the selected switching mode  $Q_g$  to find the two switching functions.
- Step 13: Reset the cost function.

Following the above 13 steps, the proposed DVV-MFPCC can be applied to the SynRM drive system whose system block diagram is shown in Figure 5.

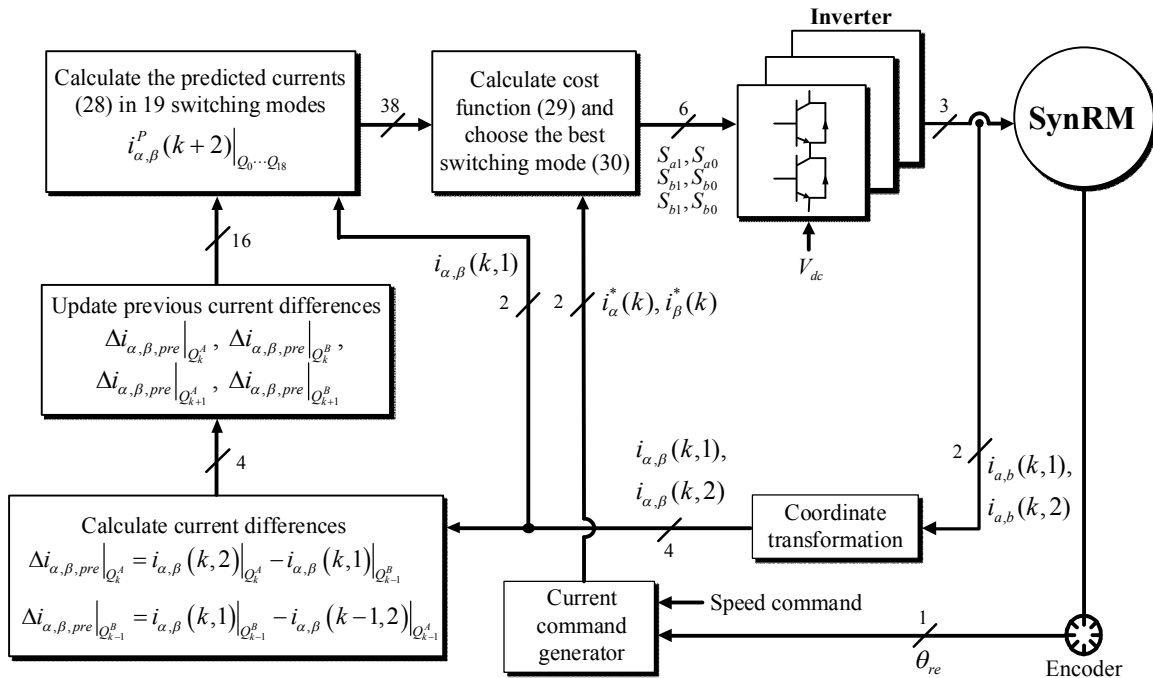


Figure 5. System block diagram of the proposed DVV-MFPCC.

## 6. Experimental Results

An experiment is conducted through a DSP TMS320F28377S where the sampling period is set as  $T_s = 100 \mu s$ . The SynRM drive system is shown in Figures 6 and 7, with its specifications listed in Table 2. The overall system consists of 9 parts: (A) DSP TMS320F28377S, (B) intelligent power module inverter, (C) two current sensors, (D) current/voltage conversion circuit, (E) 16-bit analog/digital

conversion circuit, (F) overcurrent protection circuit and encoder circuit, (G) power supply, (H) SynRM, (I) torque meter. Part B in Figure 6 is an inverter SCM1246MF (Sanken Electric Co., Ltd., Niiza-shi, Saitama-ken, Japan). The specifications of the inverter is listed in Table 3, where the rating values of main supply voltage and output current are 450 V and 30 A, respectively.

The parameters of SVV-MPCC and DVV-MPCC used in the experiments are given in Table 2. The main differences between the five predictive current controllers are listed in Table 4.

**Table 2.** Specifications of the SynRM.

Parameter	Value	Unit
Poles	8	Pole
Rated voltage	220	V
Rated power	500	W
Rated speed	1500	rpm
Stator resistance	2.5	$\Omega$
d-axis inductance	40	mH
q-axis inductance	16	mH

**Table 3.** Specifications of the inverter SCM1246MF.

Parameter	Rating Value	Unit
Main supply voltage (DC)	450	V
Main supply voltage (surge)	500	V
IGBT breakdown voltage	600	V
Output current	30	A
Output current (pulse)	45	A
Logic supply voltage	20	V
Isolation voltage (for 1 min)	2500	V

**Table 4.** The differences between five predictive current controllers.

Controller	Number of Applied Voltage Vector in One Sampling Period	Number of Current Sampling in One Sampling Period	Number of Available Switching Mode
SVV-MPCC [22]	1	1	7
DVV-MPCC	2	1	19
SVV-MFPCC [22]	1	1	7
DVV-MFPCC	2	2	19
TVB-MFPCC [23]	2	1	14

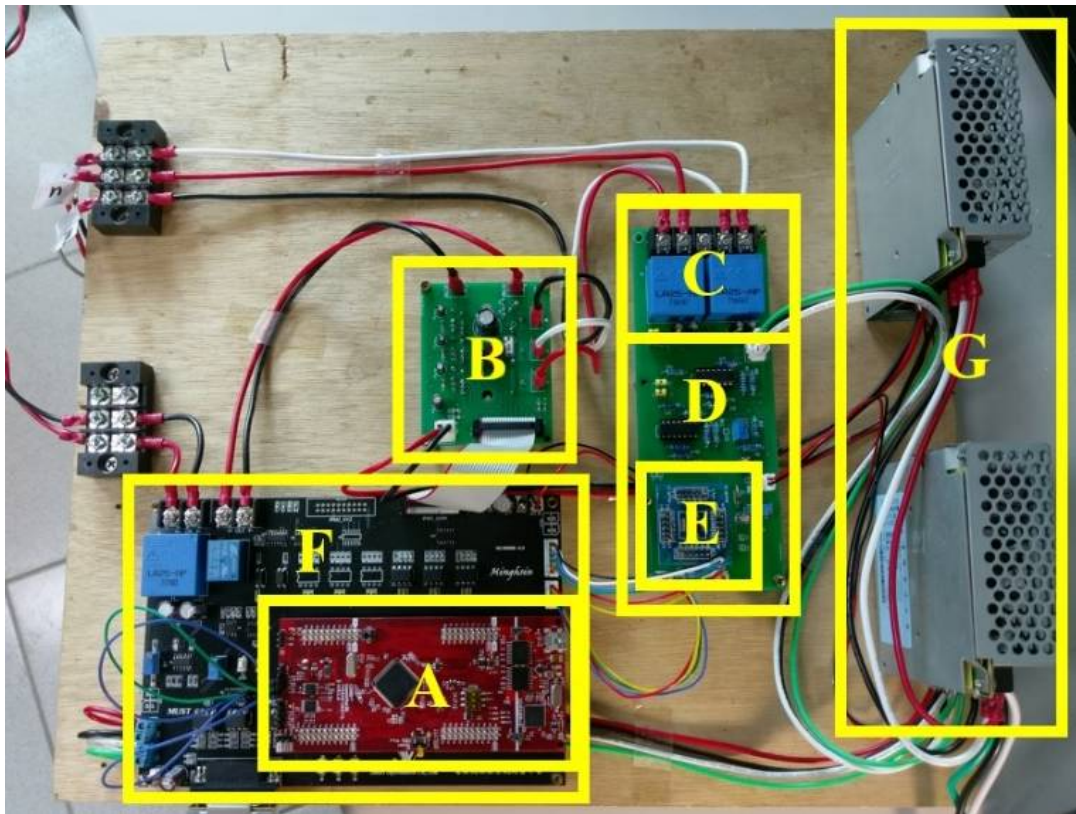


Figure 6. Hardware circuits of the SynRM drive system.

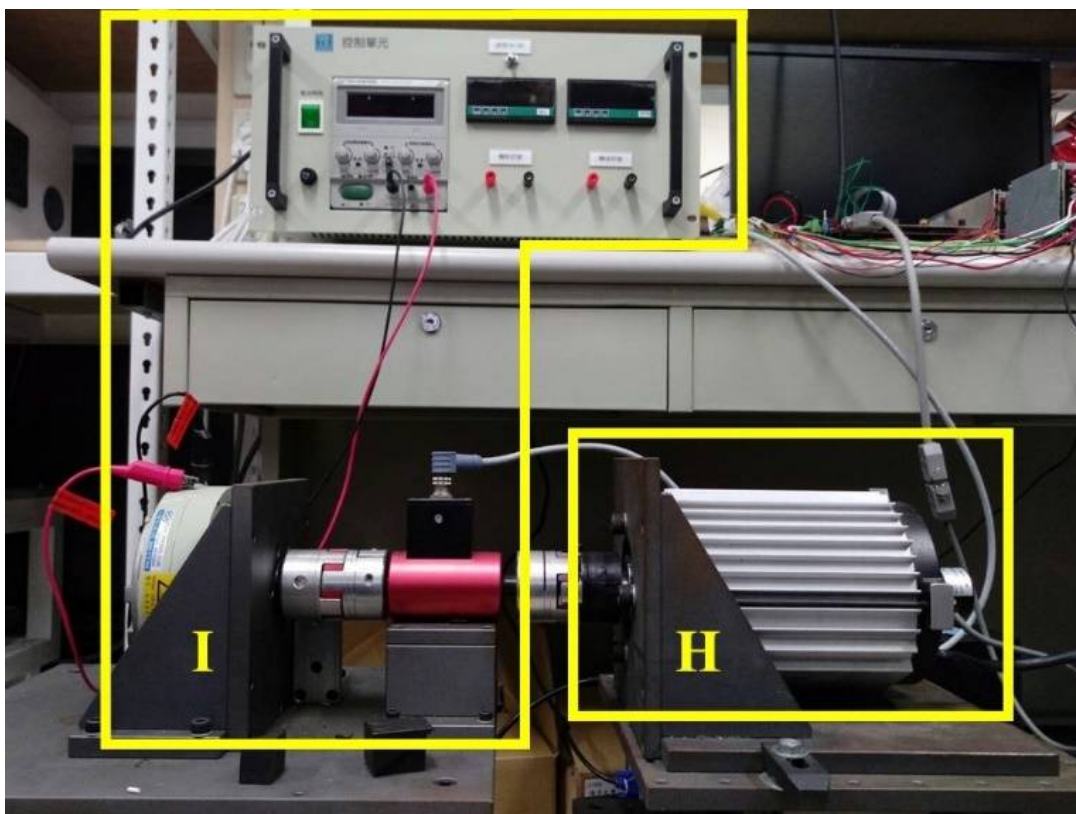


Figure 7. The SynRM connected to a torque meter.

Figures 8–27 show the experimental results of the SVV-MPCC [22], SVV-MFPCC [22], DVV-MPCC, and DVV-MFPCC to test their current-tracking performances in three cases, respectively. In Figures 8–27, the  $\alpha$ -axis and  $\beta$ -axis current errors are represented as  $e_\alpha$  and  $e_\beta$ , respectively. Five test cases are conducted under different operation conditions for the SynRM.

Case 1: To run at constant speed 300 rpm under 2 Nm load.

Case 2: To follow a sinusoidal current command with amplitude 3 A and frequency 30 Hz.

Case 3: To follow a sinusoidal current command with amplitude jumping from 2 A to 5 A at 0.1 s under frequency 10 Hz.

Case 4: To run at constant speed 1300 rpm under 1 Nm load.

Case 5: To follow a sinusoidal current command with current reversed at 0.15 s under frequency 10 Hz.

Cases 1, 2, and 4 are designed to illustrate the steady-state responses of the four PCC schemes as shown in Figures 8–15 and 20–23, while cases 3 and 5 are to show their transient responses as can be seen from Figures 16–19 and 24–27. Listed in Table 5 is the computation time. From Table 5, it can be seen that the four schemes can be executed within the sampling period, which is 100 microseconds. Among them, the DVV-MFPCC scheme requires the maximal computation time—39.6 microseconds. There are two reasons. The first of which is that the DVV-MFPCC needs two stator current measurements involving data conversion from analog into digital, which is comparatively time-consuming. In addition, as depicted by the 13 implementation steps outlined earlier, more cost value calculations as well as more updates for current differences are performed which definitely make them computationally more demanding.

In order to quantify the experimental results, three performance indexes are introduced and they are: average current error, average current ripple, and total harmonic distortion. The average current error, abbreviated as ACE, is defined as follows:

$$ACE = \frac{1}{2} \frac{1}{N} \left( \sum_{k=1}^N |i_\alpha^*[k] - i_\alpha[k]| + \sum_{k=1}^N |i_\beta^*[k] - i_\beta[k]| \right) \quad (31)$$

where the superscript “\*” represents the current command, and  $N$  stands for the number of samples. Next, the average current ripple, short as ACR, is defined by

$$ACR = \frac{1}{2} \left( \sqrt{\frac{1}{N} \sum_{k=1}^N (i_\alpha^*[k] - i_\alpha[k])^2} + \sqrt{\frac{1}{N} \sum_{k=1}^N (i_\beta^*[k] - i_\beta[k])^2} \right) \quad (32)$$

As the last performance index, the average total harmonic distortion, denoted as ATHD, can be calculated by

$$ATHD = \frac{1}{2} \left( \frac{\sqrt{\sum_{n=2}^{30} I_{n,\alpha}^2}}{I_{1,\alpha,rms}} + \frac{\sqrt{\sum_{n=2}^{30} I_{n,\beta}^2}}{I_{1,\beta,rms}} \right) \quad (33)$$

where the first subscript symbol “ $n$ ” represents the  $n$ th harmonic component and the second subscript “ $\alpha$ ” or “ $\beta$ ” means the current of  $\alpha$ -axis or  $\beta$ -axis. Quantified results of Figures 8–11, Figures 12–15, Figures 16–19, Figures 20–23, and Figures 24–27 are provided in Tables 6–10, respectively, following Equations (31)–(33). As one can observe from Figures 8–11 and Table 6, the proposed DVV-MFPCC has the lowest ACE, ACR, and ATHD in case 1. For case 2, the proposed DVV-MFPCC has the lowest ACR and ATHD as can be seen from Table 7 and Figures 12–15. The results of case 3, as shown in Figures 16–19 and Table 8, for the transient responses depict that the DVV-MFPCC has the minimum values of ACE, ACR, and ATHD.

Figures 20–23 show the current responses of the four PCCs under 1300 rpm and 1 Nm load as case 4 whose performance indexes are listed in Table 9. Since the drive system used in this study is not

a commercial one but rather a prototype designed and developed by the authors, inherently it may have certain limitations in regard to the rated speed.

The experimental results of case 5 are shown in Figures 24–27 and Table 10. Ideally, the stator current of the SynRM can be predicted by DVV-MPCC well if the used mathematical model perfectly matches the actual motor and the back EMF estimation will be perfect. It is worth mentioning that the mathematical model of SynRM is coupled and nonlinear [22]. The DVV-MPCC is based on a decoupled model like the SVV-MPCC from [6]. In order for DVV-MPCC to be applicable to the SynRM, the equivalent stator voltage Equations (1) and (2) make some assumptions, such as zero magnetic saturation, zero eddy current, and zero hysteresis loss inevitably leading to some model errors. In addition, the parameters of the SynRM listed in Table 2 will also vary under different operation conditions. For example, the stator resistance will change at different temperatures, and the inductance value will also vary at different currents and frequencies. Moreover, since the back EMF in Equation (18) is obtained by estimation rather than through instrumental measurement, its estimation error always exists and is unavoidable. Unlike DVV-MPCC, the DVV-MFPCC is based on Equation (28), implying that no mathematical model and motor parameters are needed as the stator current can be accurately measured through current sensor. As long as the microcontroller works properly under a sufficiently short sampling period, the previous current differences required in Equation (28) can be updated frequently to reduce errors. As such, the DVV-MFPCC, as compared to the DVV-MPCC, is expected to perform better.

In summary, the experimental results demonstrate that the DVV-MFPCC presented in this work indeed performs better in terms of the steady-state and transient responses.

**Table 5.** Computation time for different schemes using the microcontroller TMS320F28377S.

PCC Scheme	Computation Time ( $\mu\text{s}$ )
SVV-MPCC [22]	20
DVV-MPCC	29
SVV-MFPCC [22]	19.8
DVV-MFPCC	39.6

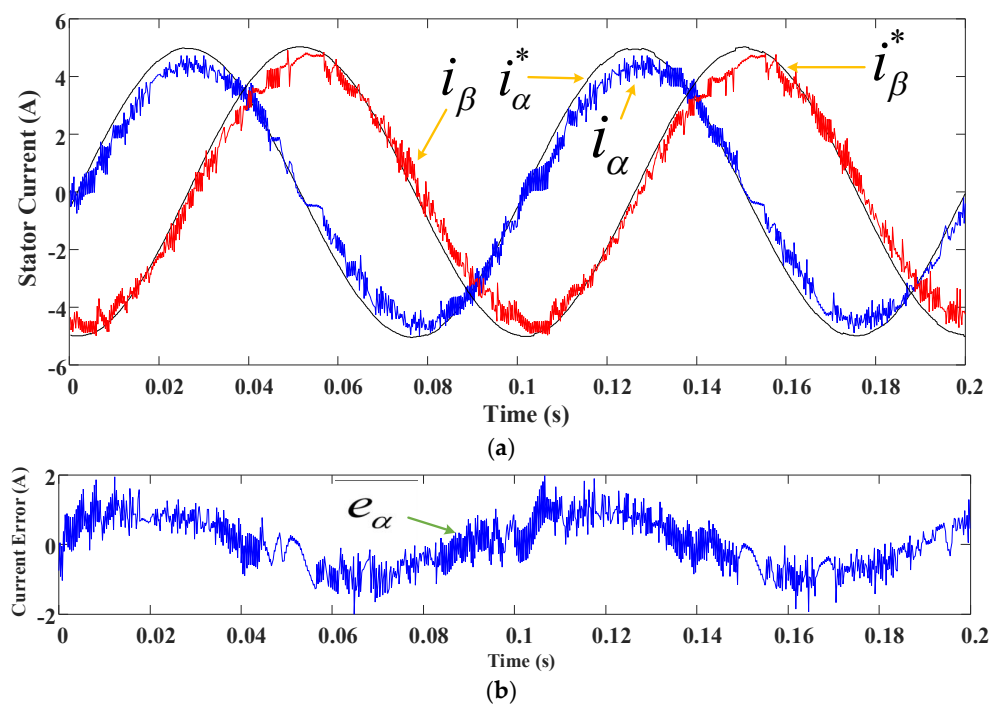


**Figure 8.** Cont.

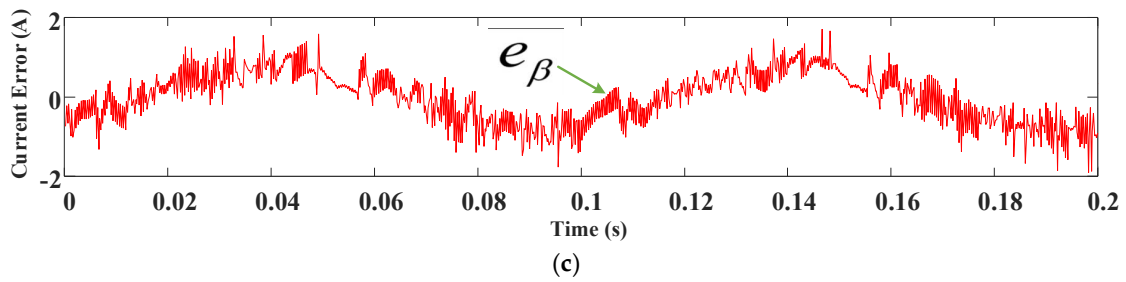


Figure 8. Experimental results of SVV-MPCC under speed 300 rpm and load 2 Nm (case 1): (a) current responses; (b)  $\alpha$ -axis current error; (c)  $\beta$ -axis current error.

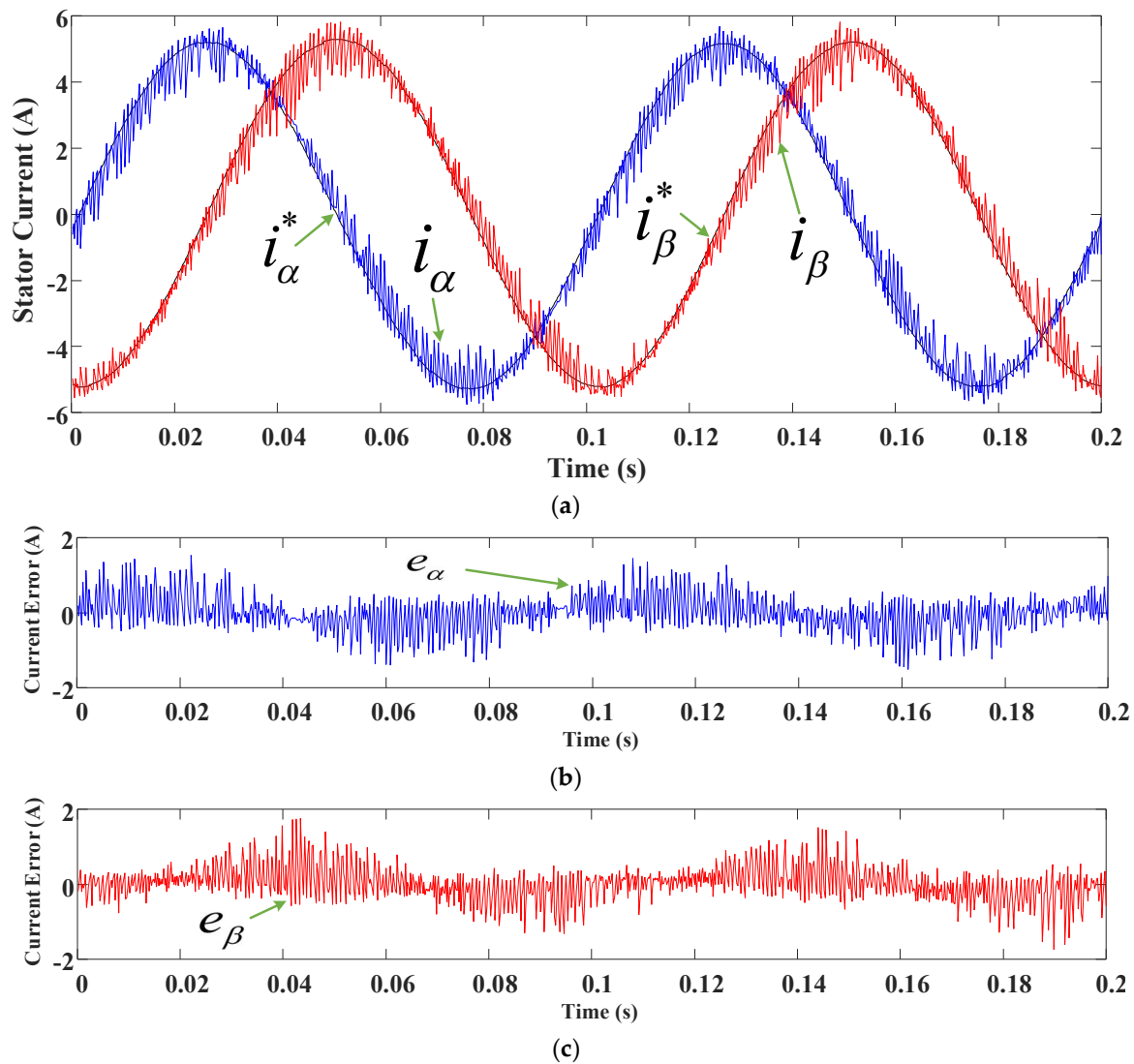


Figure 9. Experimental results of DVV-MPCC under speed 300 rpm and load 2 Nm (case 1): (a) current responses; (b)  $\alpha$ -axis current error; (c)  $\beta$ -axis current error.

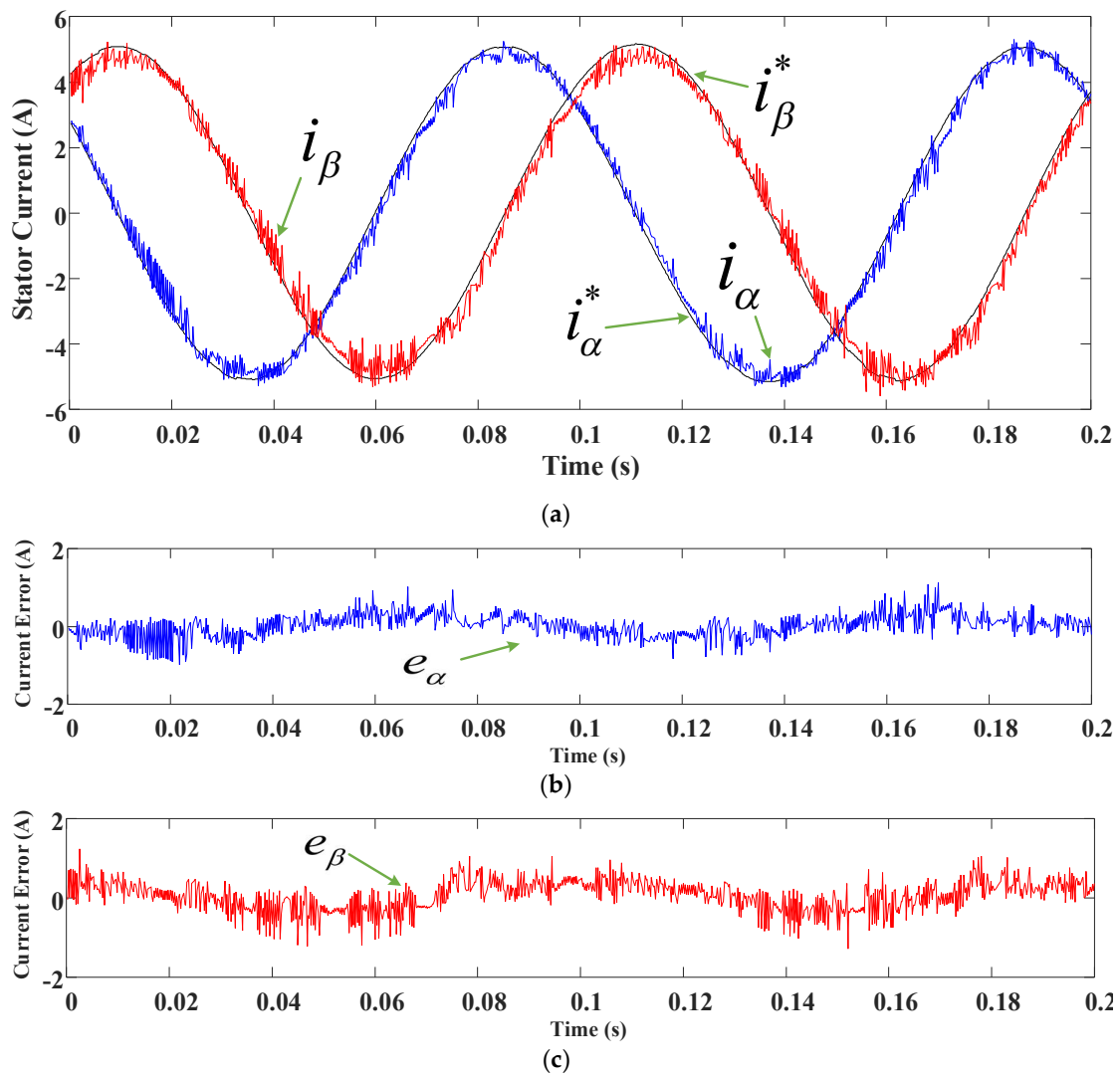


Figure 10. Experimental results of SVV-MFPC under speed 300 rpm and load 2 Nm (case 1): (a) current responses; (b)  $\alpha$ -axis current error; (c)  $\beta$ -axis current error.

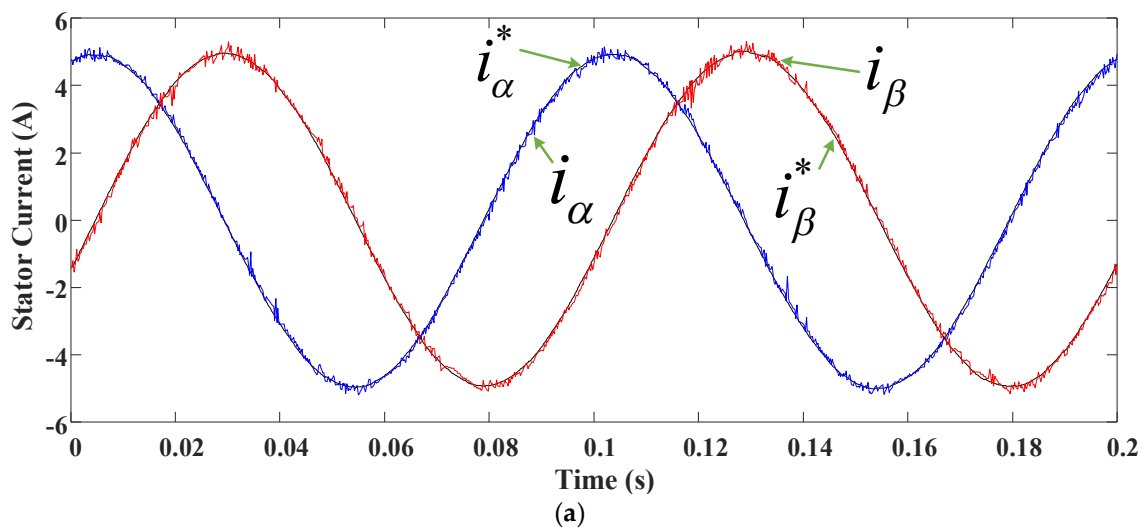
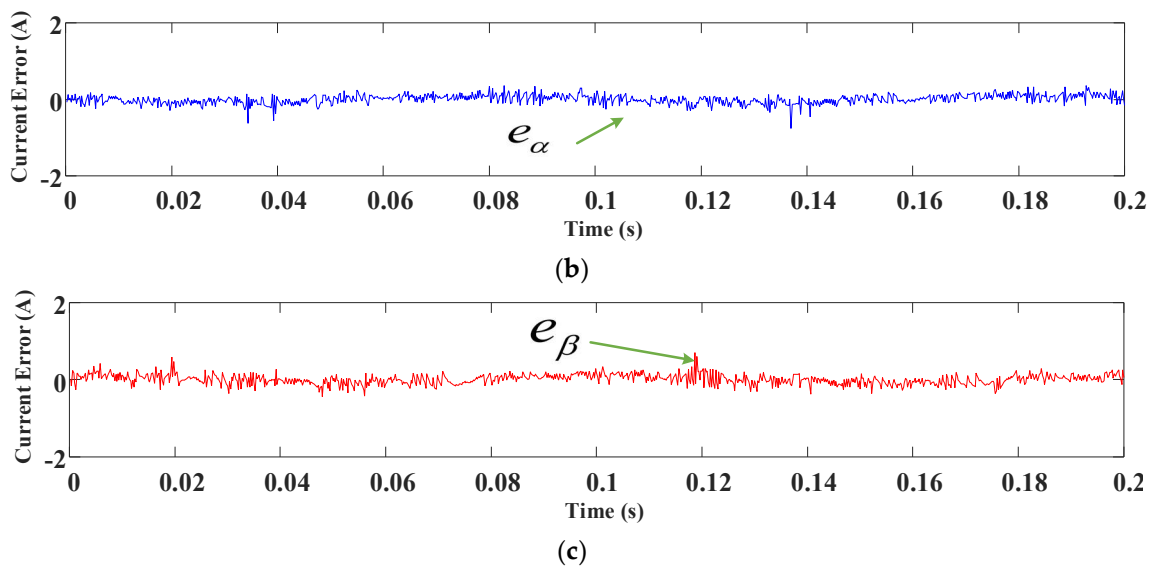
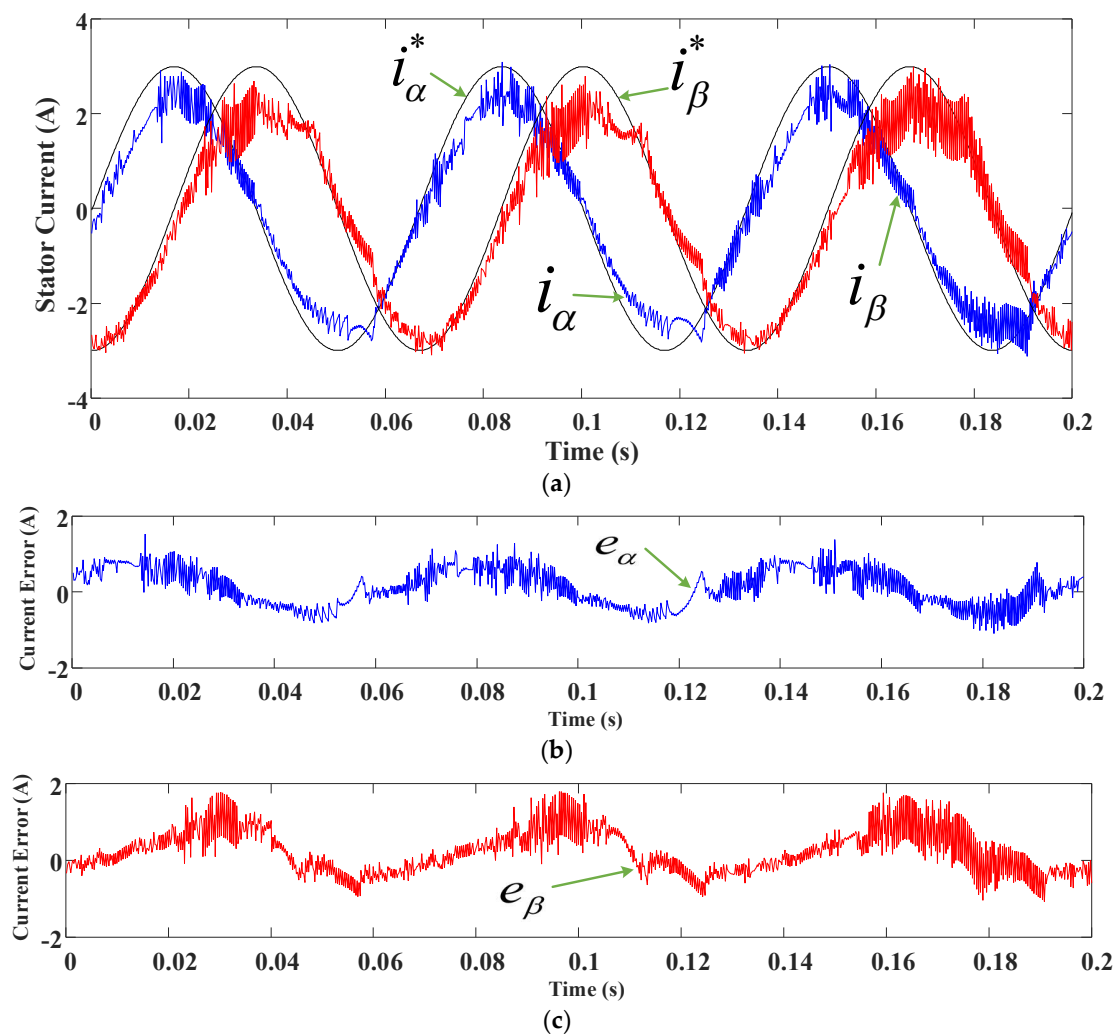


Figure 11. Cont.



**Figure 11.** Experimental results of DVV-MFPCC under speed 300 rpm and load 2 Nm (case 1): (a) current responses; (b)  $\alpha$ -axis current error; (c)  $\beta$ -axis current error.



**Figure 12.** Experimental results of SVV-MPCC following a sinusoidal current command with amplitude 3 A and frequency 30 Hz (case 2): (a) current responses; (b)  $\alpha$ -axis current error; (c)  $\beta$ -axis current error.

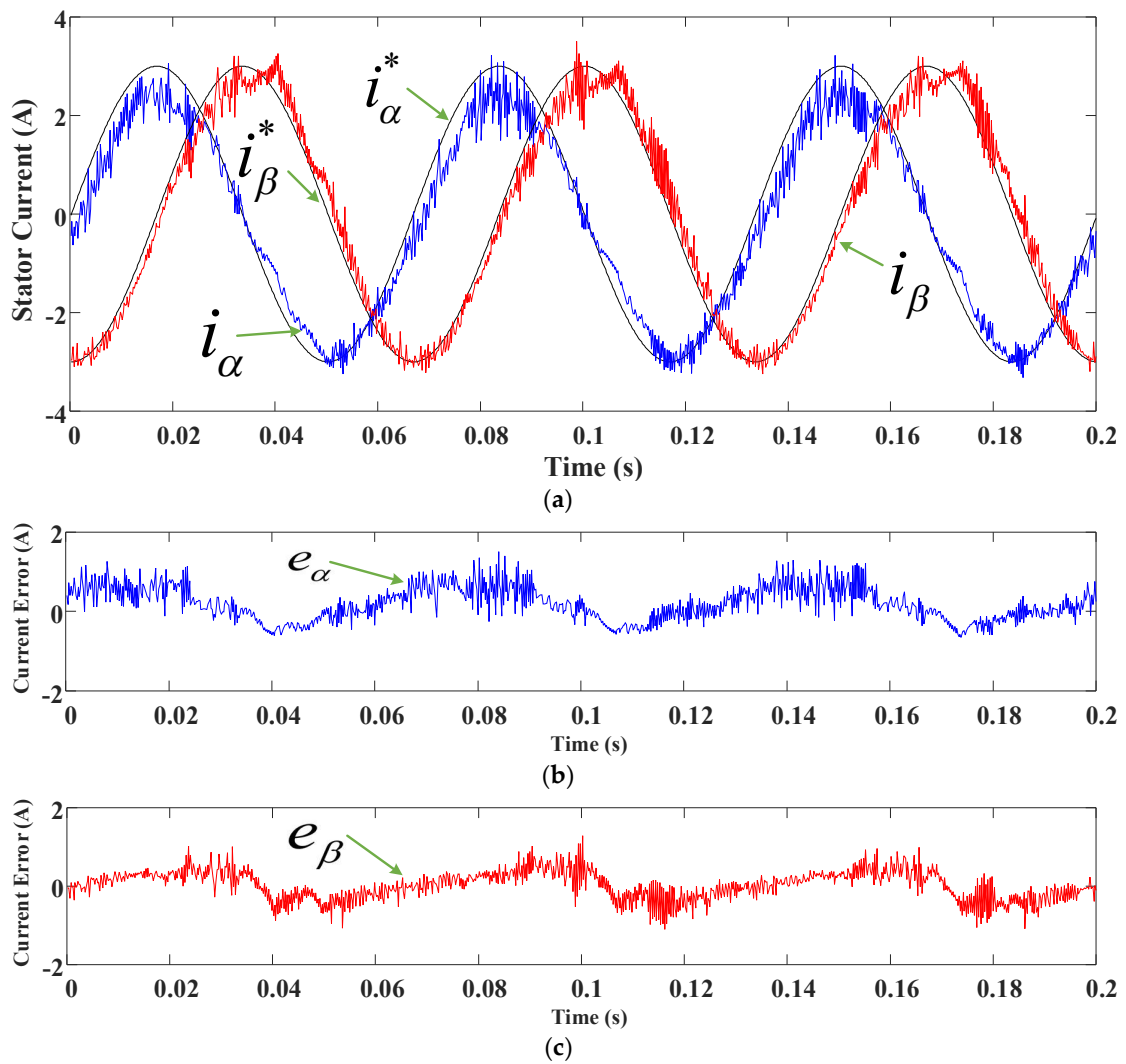


**Figure 13.** Experimental results of DVV-MPCC following a sinusoidal current command with amplitude 3 A and frequency 30 Hz (case 2): (a) current responses; (b)  $\alpha$ -axis current error; (c)  $\beta$ -axis current error.

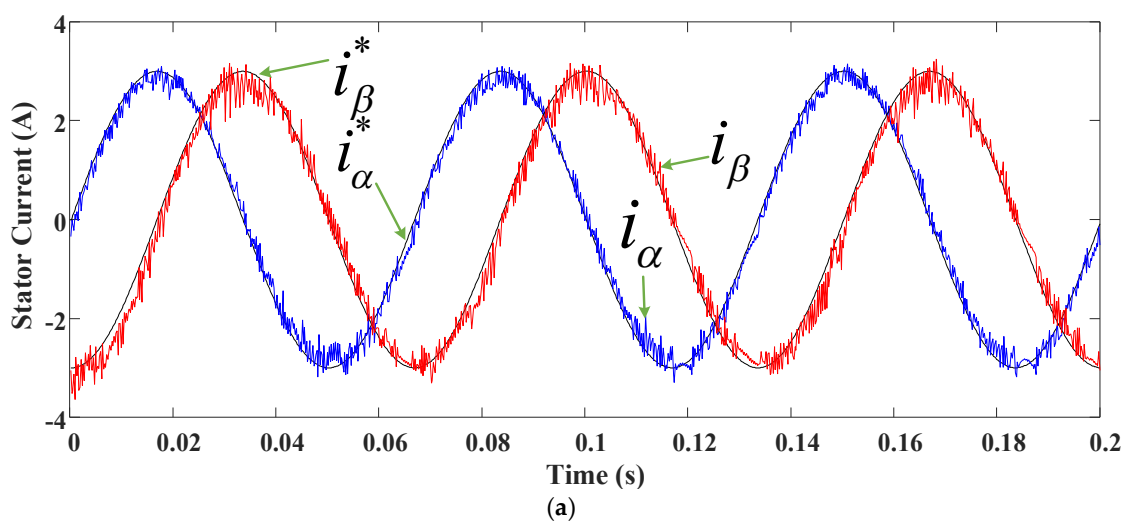


**Figure 14.** Cont.

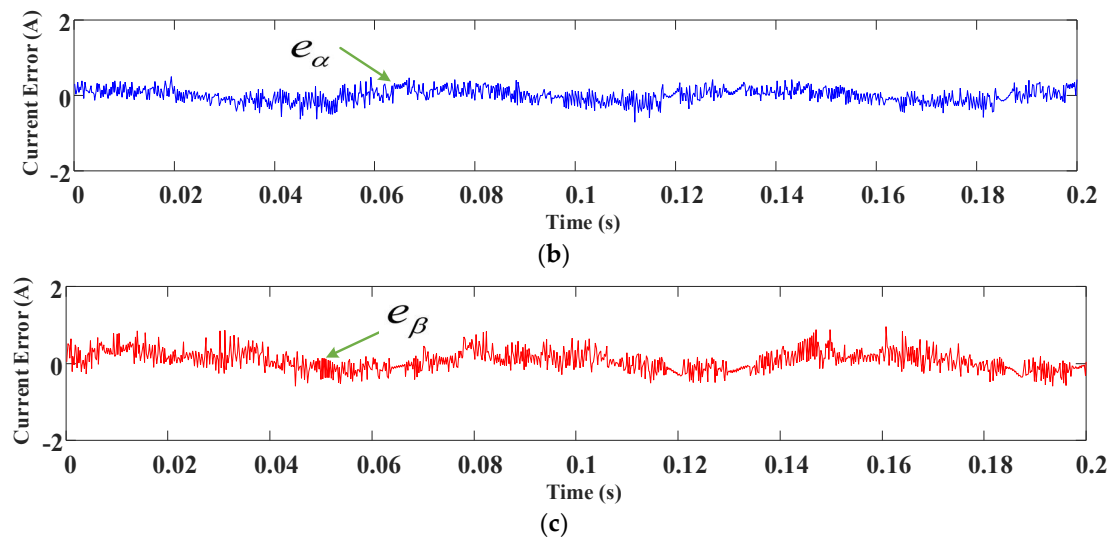


**Figure 14.** Experimental results of SVV-MFPCC following a sinusoidal current command with amplitude 3 A and frequency 30 Hz (case 2): (a) current responses; (b)  $\alpha$ -axis current error; (c)  $\beta$ -axis current error.

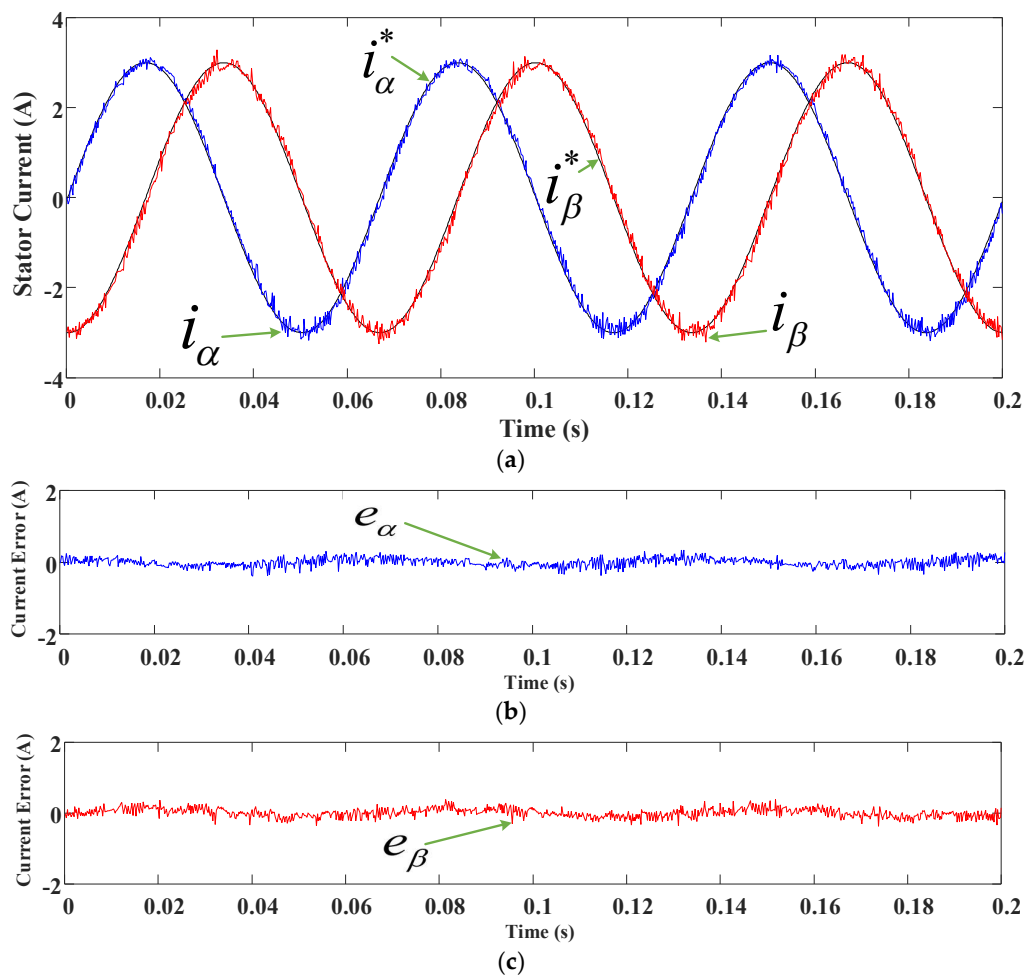


**Figure 15.** Experimental results of DVV-MFPCC following a sinusoidal current command with amplitude 3 A and frequency 30 Hz (case 2): (a) current responses; (b)  $\alpha$ -axis current error; (c)  $\beta$ -axis current error.

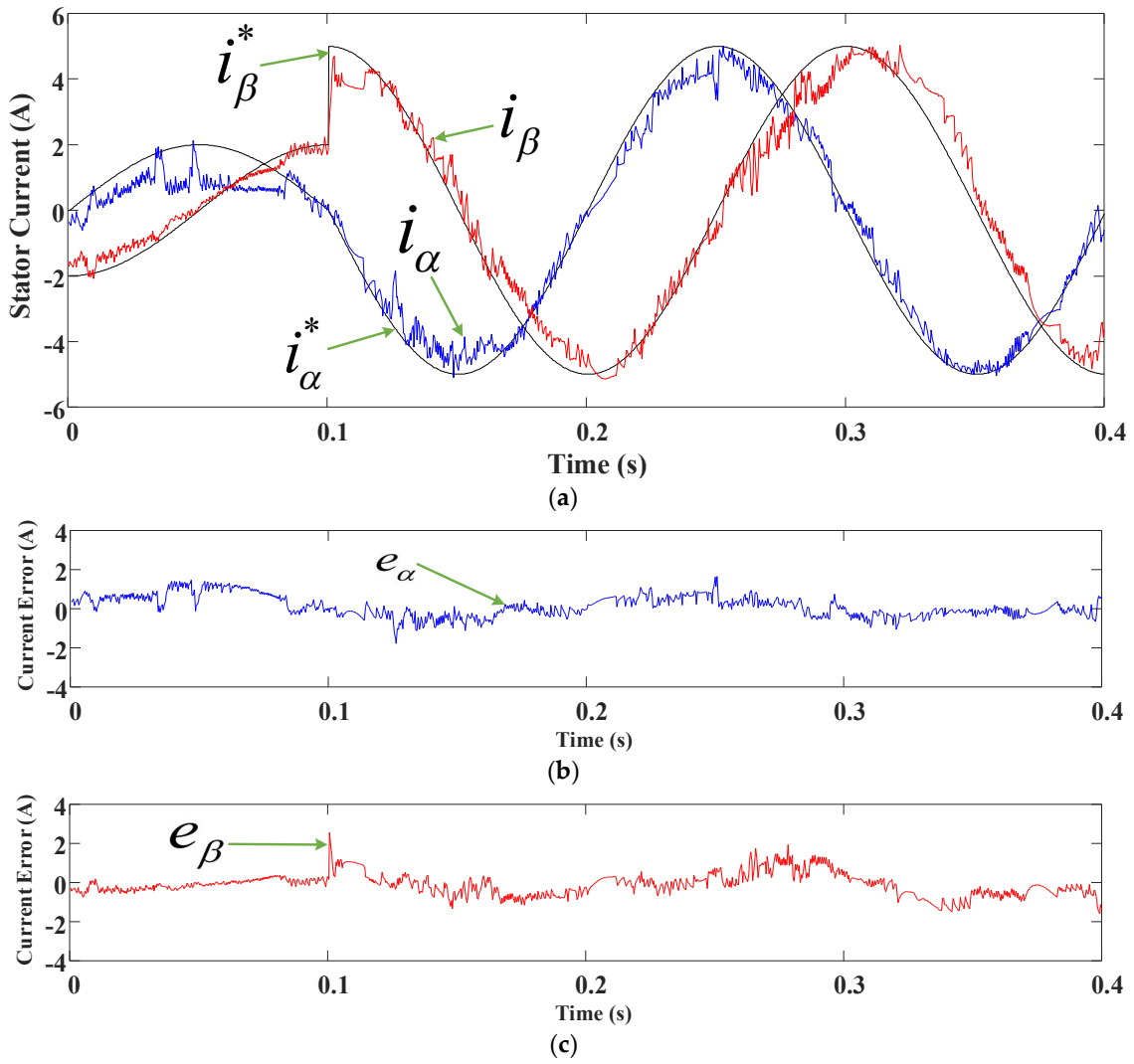


**Figure 16.** Experimental results of SVV-MPCC following a sinusoidal current command with amplitude jumping from 2 A to 5 A at 0.1 s under frequency 10 Hz (case 3): (a) current responses; (b)  $\alpha$ -axis current error; (c)  $\beta$ -axis current error.

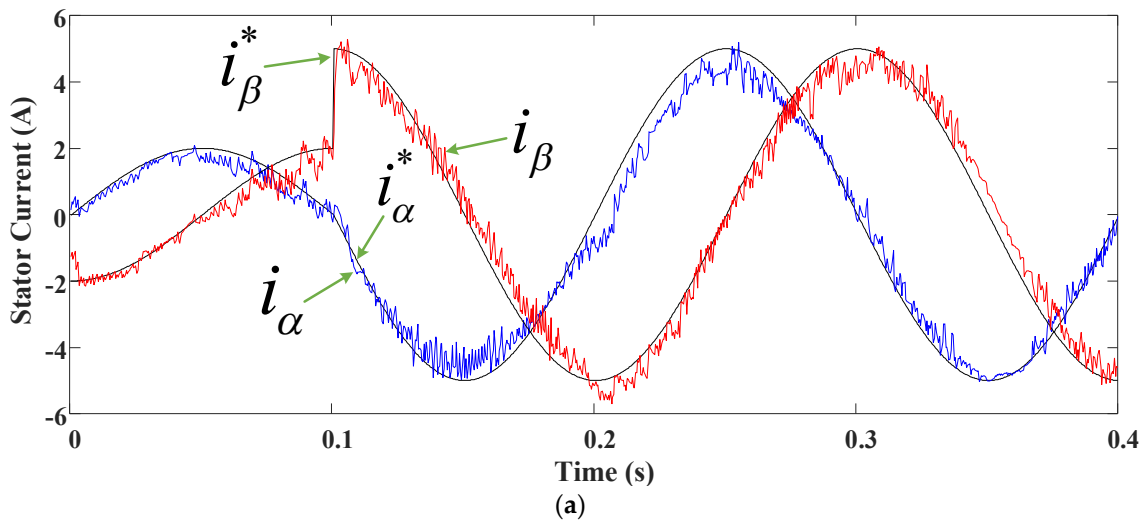


**Figure 17.** Cont.

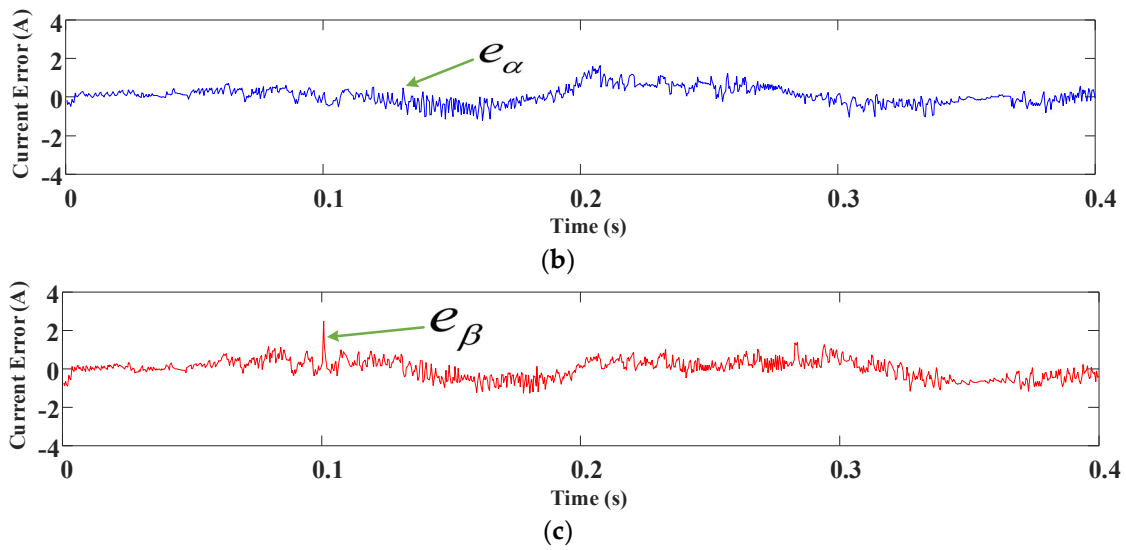


**Figure 17.** Experimental results of DVV-MPCC following a sinusoidal current command with amplitude jumping from 2 A to 5 A at 0.1 s under frequency 10 Hz (case 3): (a) current responses; (b)  $\alpha$ -axis current error; (c)  $\beta$ -axis current error.

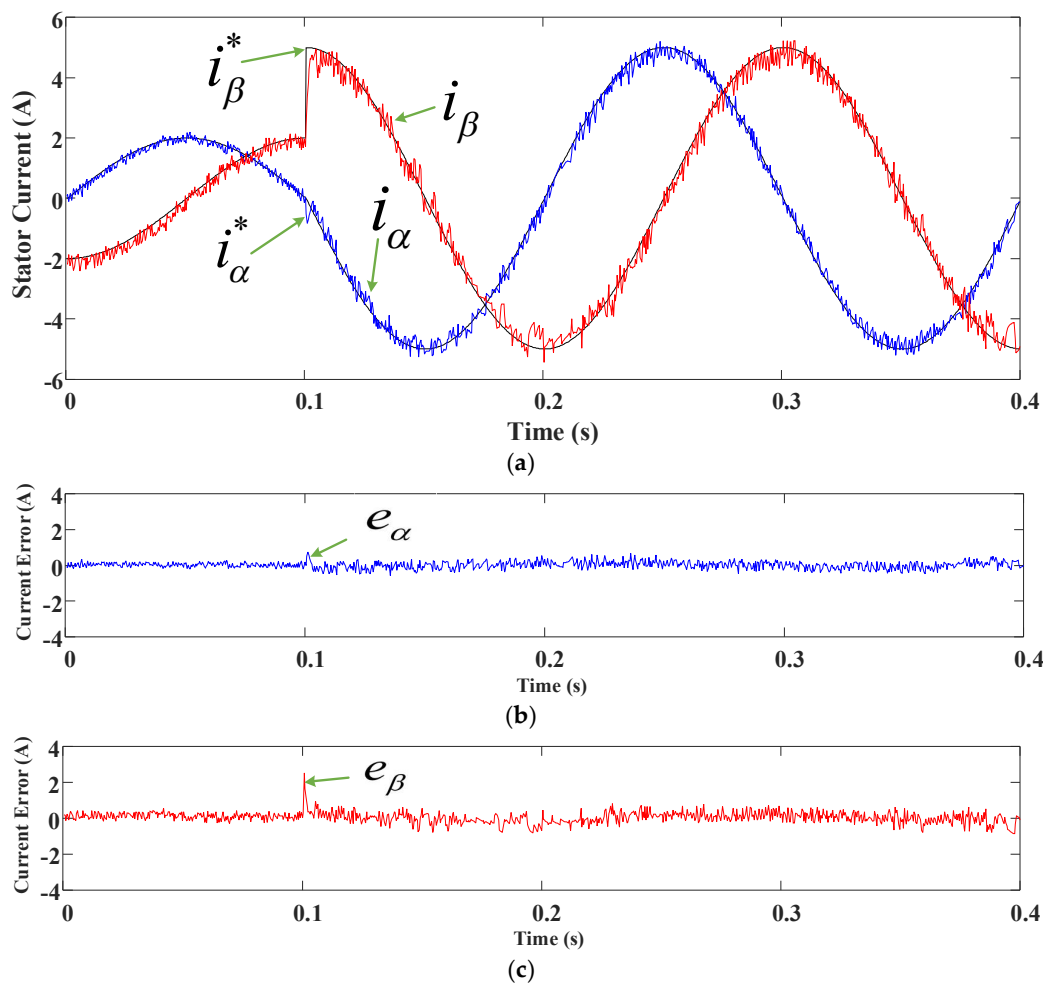


**Figure 18.** Experimental results of SVV-MFPCC following a sinusoidal current command with amplitude jumping from 2 A to 5 A at 0.1 s under frequency 10 Hz (case 3): (a) current responses; (b)  $\alpha$ -axis current error; (c)  $\beta$ -axis current error.

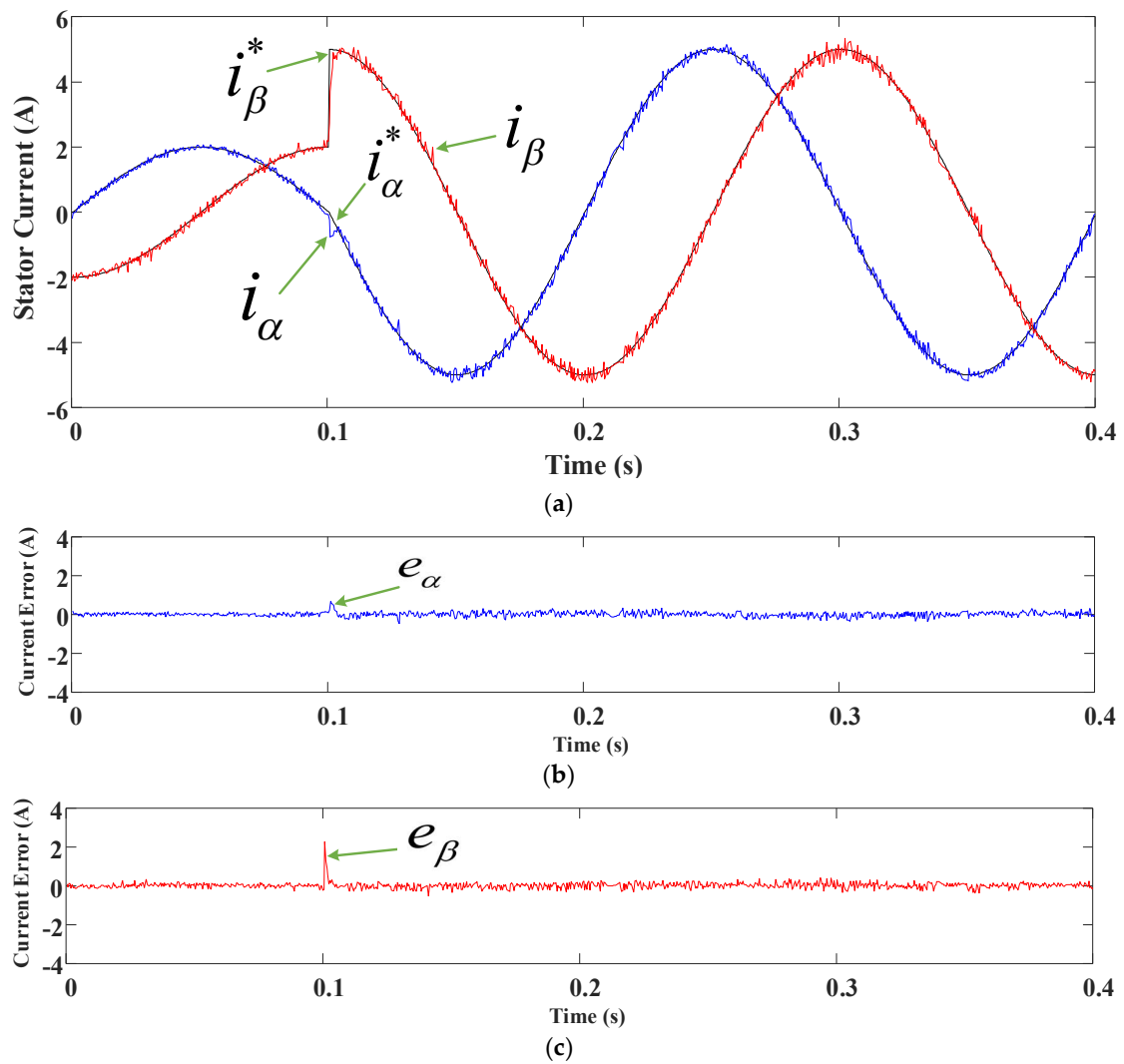


Figure 19. Experimental results of DVV-MFPC following a sinusoidal current command with amplitude jumping from 2 A to 5 A at 0.1 s under frequency 10 Hz (case 3): (a) current responses; (b)  $\alpha$ -axis current error; (c)  $\beta$ -axis current error.

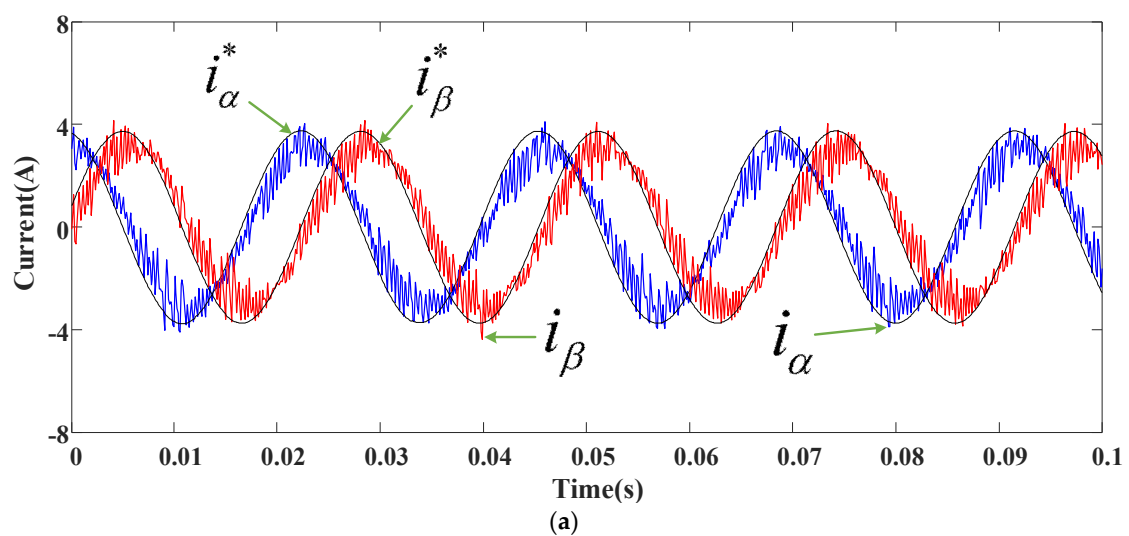
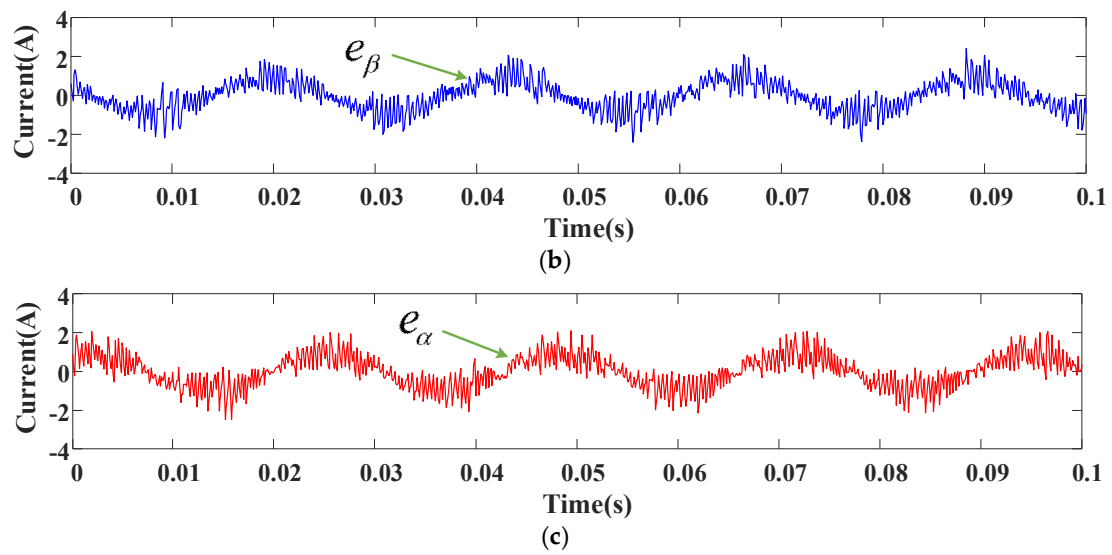
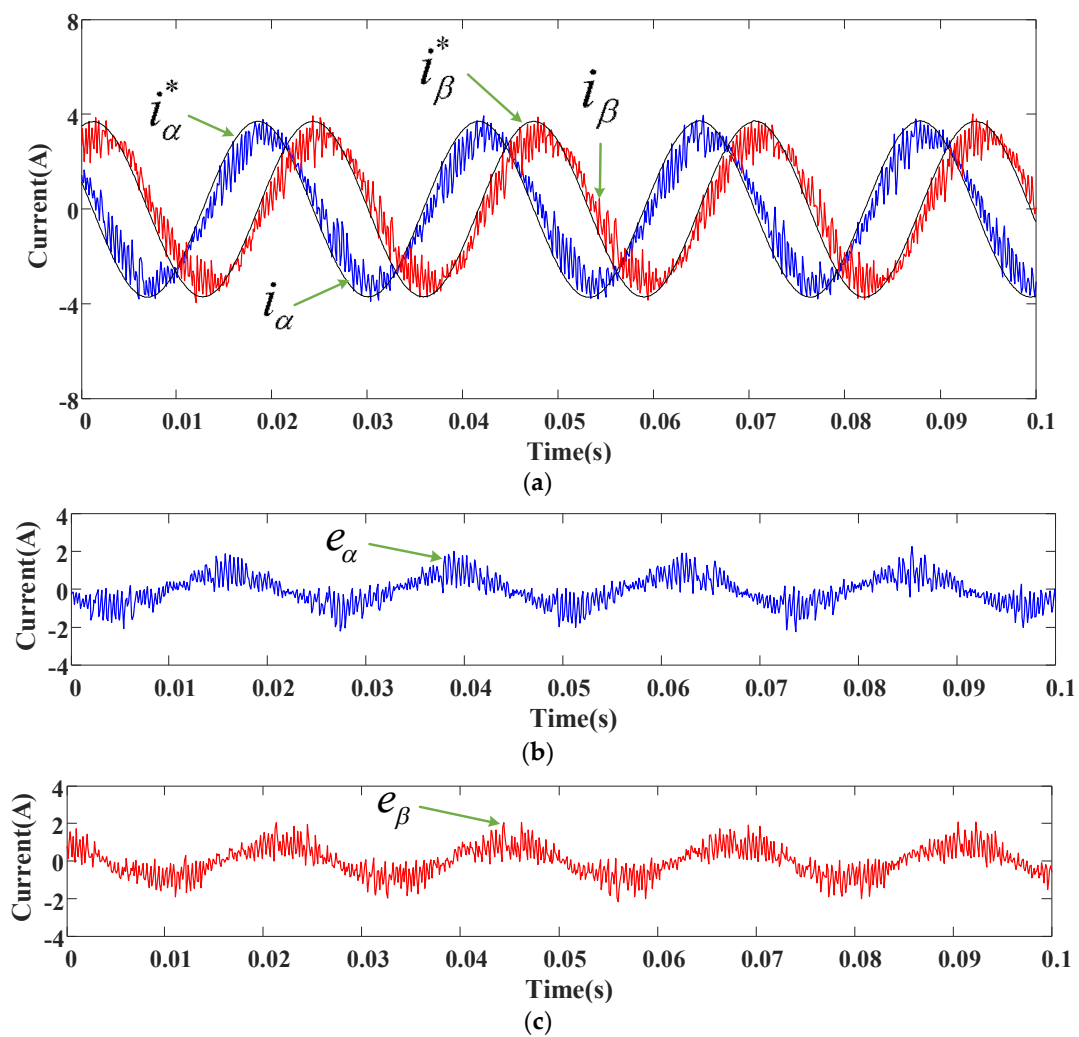


Figure 20. Cont.



**Figure 20.** Experimental results of SVV-MPCC under speed 1300 rpm and load 1 Nm (case 4): (a) current responses; (b)  $\alpha$ -axis current error; (c)  $\beta$ -axis current error.



**Figure 21.** Experimental results of DVV-MPCC under speed 1300 rpm and load 1 Nm (case 4): (a) current responses; (b)  $\alpha$ -axis current error; (c)  $\beta$ -axis current error.

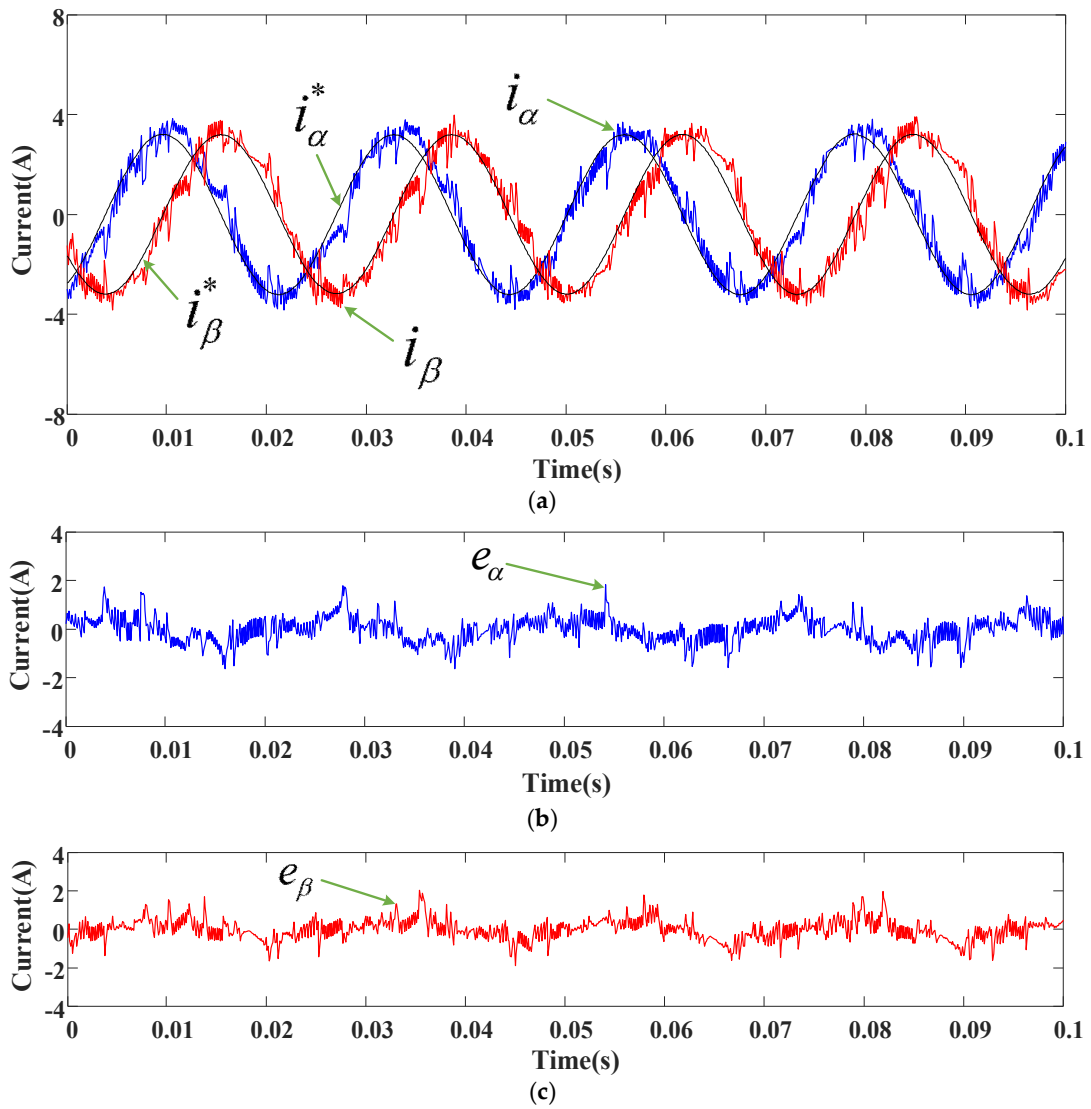


Figure 22. Experimental results of SVV-MFPC under speed 1300 rpm and load 1 Nm (case 4): (a) current responses; (b)  $\alpha$ -axis current error; (c)  $\beta$ -axis current error.

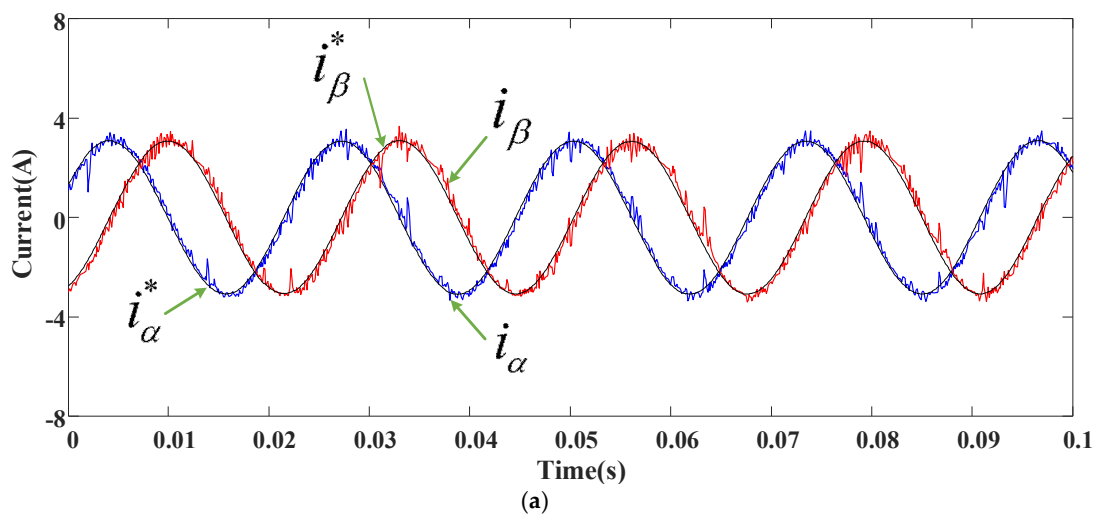
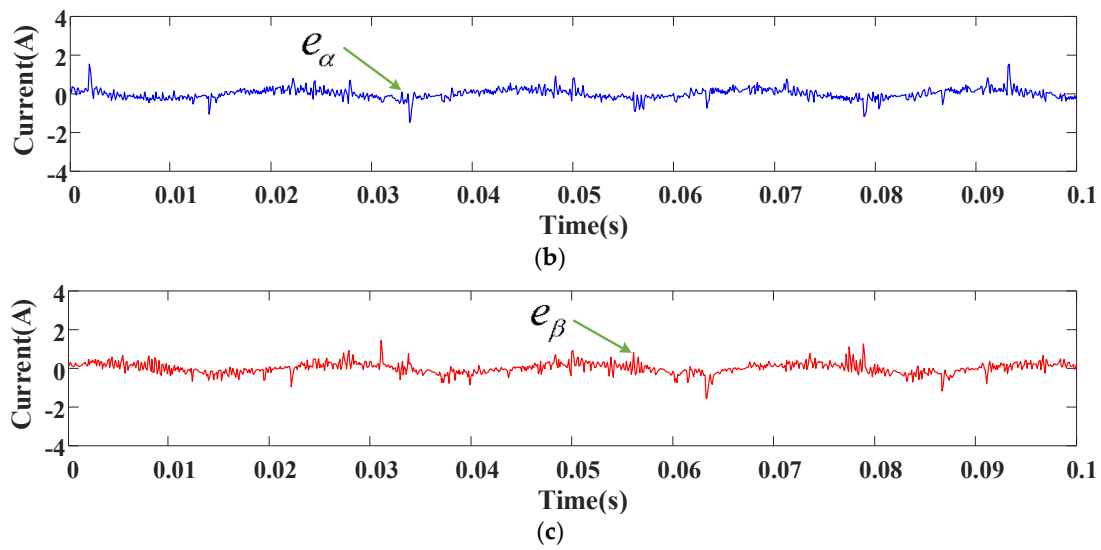
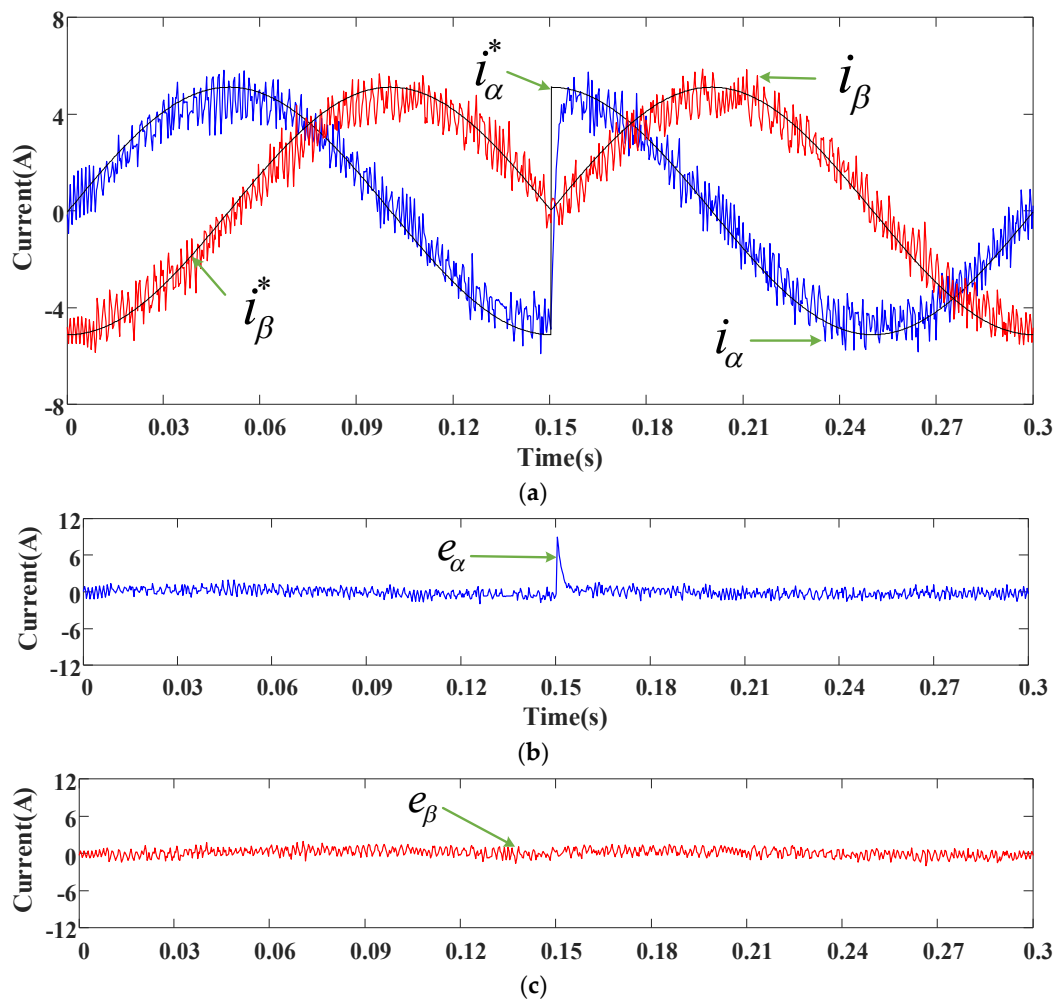


Figure 23. Cont.



**Figure 23.** Experimental results of DVV-MFPC under speed 1300 rpm and load 1 Nm (case 4): (a) current responses; (b)  $\alpha$ -axis current error; (c)  $\beta$ -axis current error.



**Figure 24.** Experimental results of SVV-MPCC following a sinusoidal current command with current reversed at 0.15 s under frequency 10 Hz (case 5): (a) current responses; (b)  $\alpha$ -axis current error; (c)  $\beta$ -axis current error.

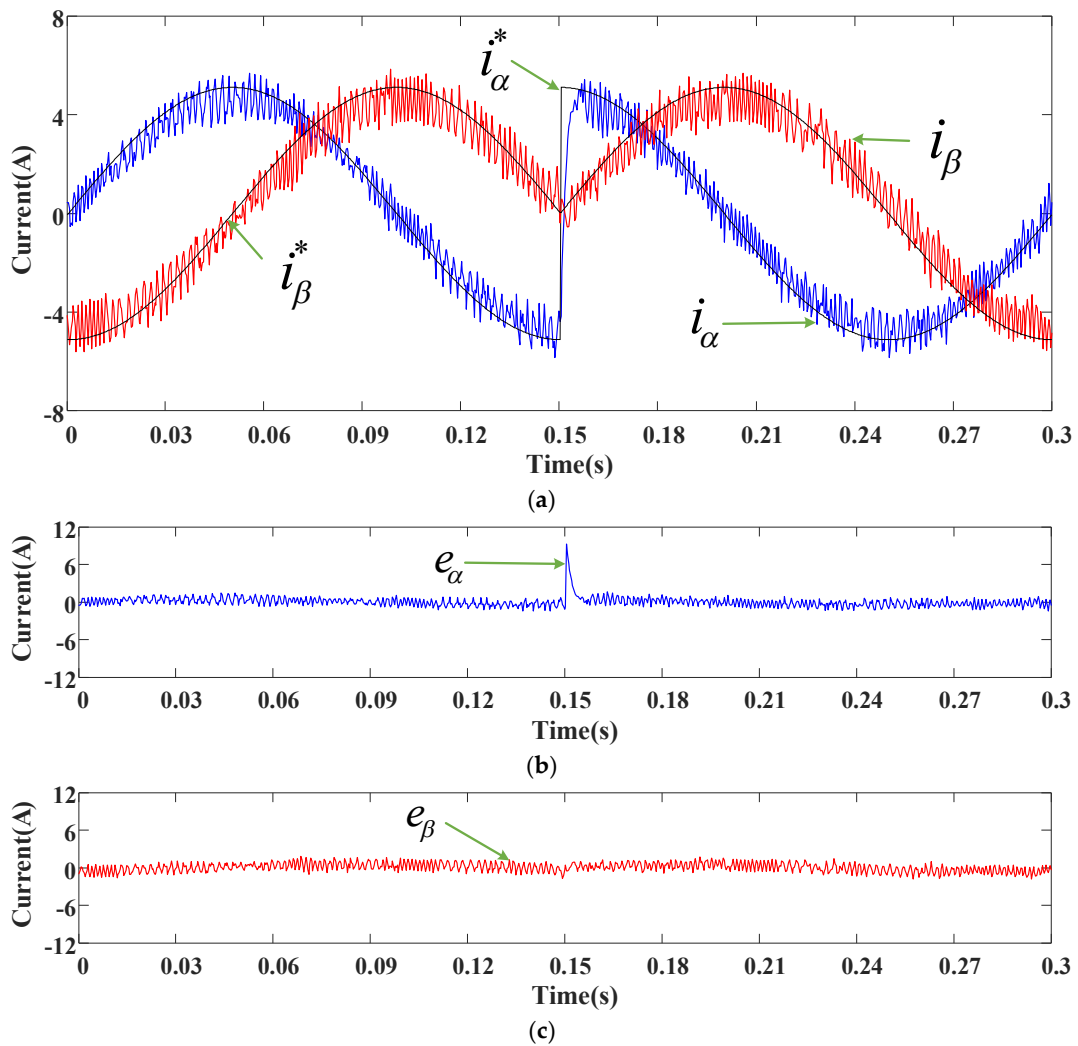


**Figure 25.** Experimental results of DVV-MPCC following a sinusoidal current command with current reversed at 0.15 s under frequency 10 Hz (case 5): (a) current responses; (b)  $\alpha$ -axis current error; (c)  $\beta$ -axis current error.

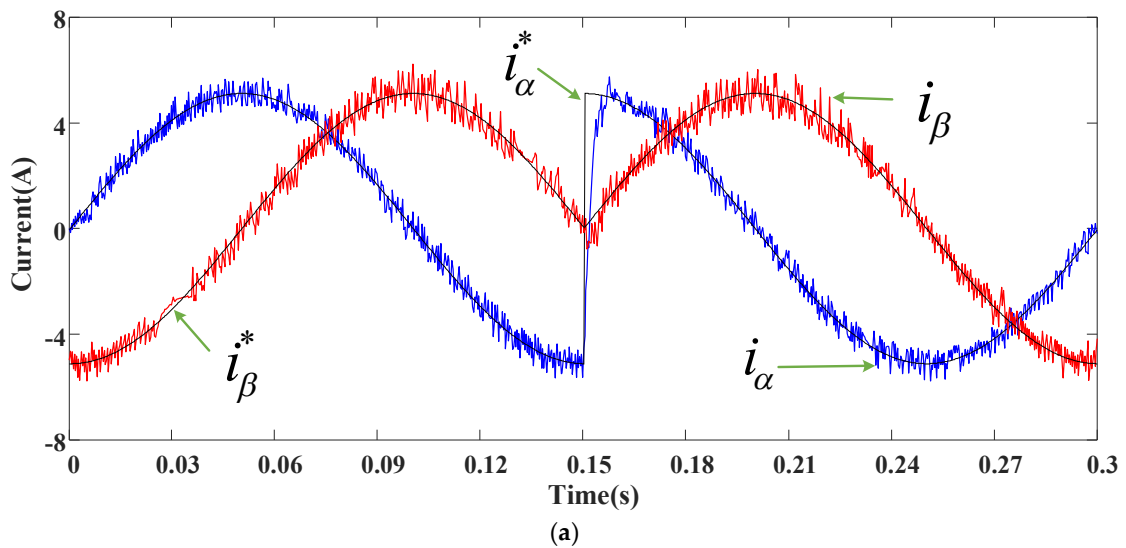


**Figure 26.** Cont.

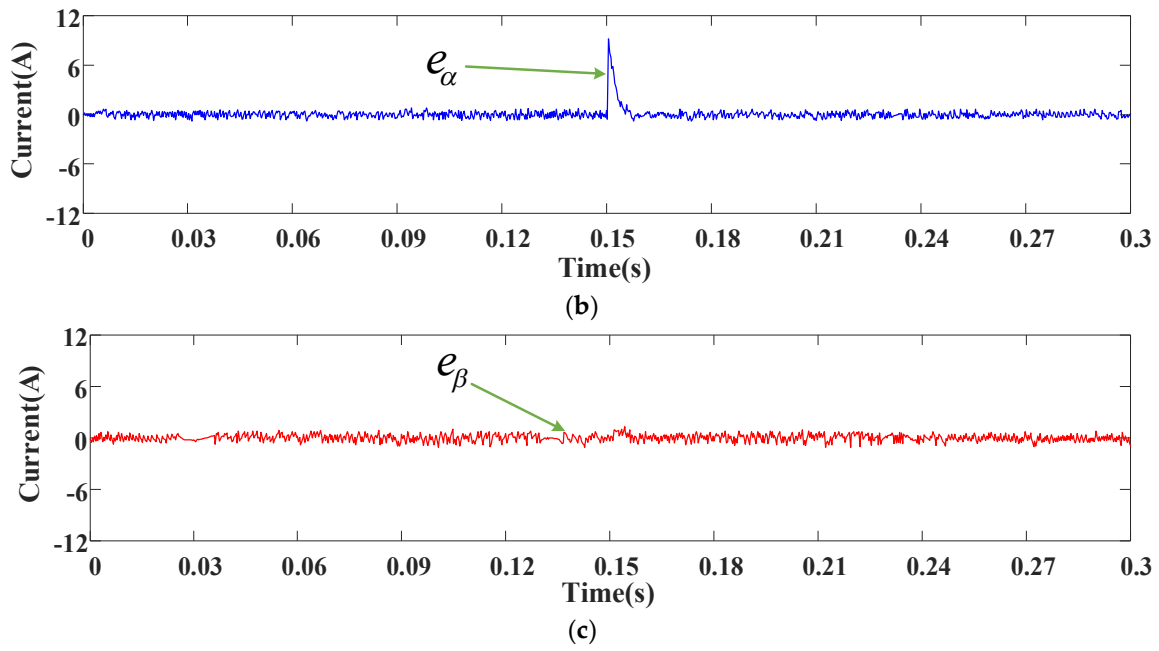


Figure 26. Experimental results of SVV-MFPC following a sinusoidal current command with current reversed at 0.15 s under frequency 10 Hz (case 5): (a) current responses; (b)  $\alpha$ -axis current error; (c)  $\beta$ -axis current error.

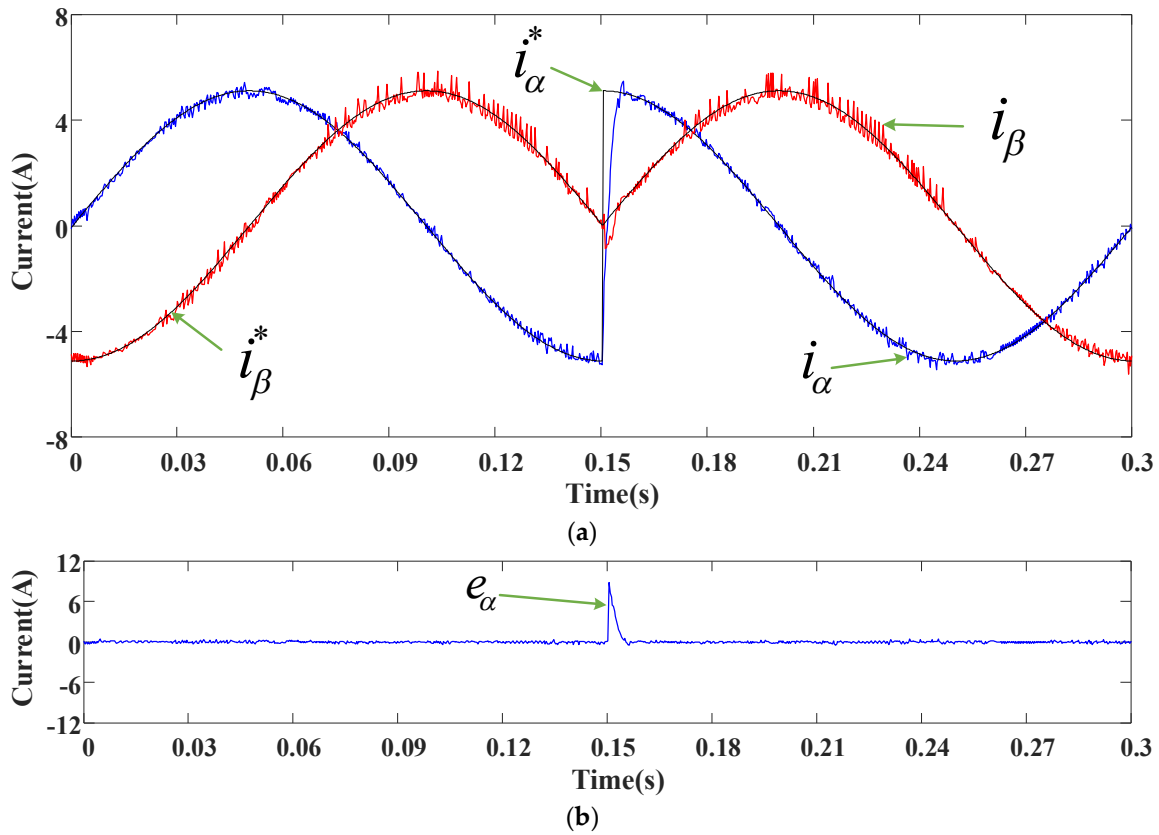
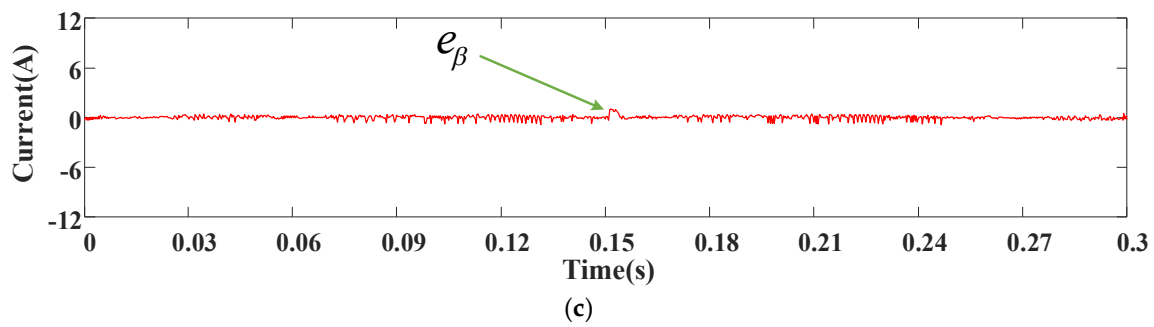


Figure 27. Cont.



**Figure 27.** Experimental results of DVV-MFPCC following a sinusoidal current command with current reversed at 0.15 s under frequency 10 Hz (case 5): (a) current responses; (b)  $\alpha$ -axis current error; (c)  $\beta$ -axis current error.

**Table 6.** ACE, ACR, and ATHD of the four schemes obtained from Figures 8–11.

Scheme	ACE (A)	ACR (A)	ATHD (%)
SVV-MPCC	0.666	0.668	2.949
DVV-MPCC	0.672	0.466	1.737
SVV-MFPCC	0.280	0.350	2.071
DVV-MFPCC	0.102	0.126	0.863

**Table 7.** ACE, ACR, and ATHD of the four schemes obtained from Figures 12–15.

PCC Scheme	ACE (A)	ACR (A)	ATHD (%)
SVV-MPCC	0.480	0.575	2.956
DVV-MPCC	0.171	0.421	2.960
SVV-MFPCC	0.285	0.243	1.989
DVV-MFPCC	0.182	0.124	1.202

**Table 8.** ACE, ACR, and ATHD of the four schemes obtained from Figures 16–19.

PCC Scheme	ACE (A)	ACR (A)	ATHD (%)
SVV-MPCC	0.961	0.570	8.896
DVV-MPCC	0.243	0.466	10.010
SVV-MFPCC	0.069	0.260	7.693
DVV-MFPCC	0.059	0.139	7.626

**Table 9.** ACE, ACR, and ATHD of the four schemes obtained from Figures 20–23.

PCC Scheme	ACE (A)	ACR (A)	ATHD (%)
SVV-MPCC	0.64	0.814	11.678
DVV-MPCC	0.613	0.78	10.441
SVV-MFPCC	0.432	0.554	10.208
DVV-MFPCC	0.21	0.283	9.783

**Table 10.** ACE, ACR, and ATHD of the four schemes obtained from Figures 24–27.

PCC Scheme	ACE (A)	ACR (A)	ATHD (%)
SVV-MPCC	0.55	0.731	23.11
DVV-MPCC	0.55	0.738	23.269
SVV-MFPCC	0.333	0.534	23.399
DVV-MFPCC	0.167	0.4	23.149

## 7. Conclusions

The proposed DVV-MFPCC is successfully implemented on a SynRM drive system. In each sampling period two voltage vectors rather than one are applied. The number of candidate switching modes is increased to nineteen. In addition, the stator current is measured twice in each sampling period. Finally, compared to the SVV-MPCC, the SVV-MFPCC, and the DVV-MPCC, the experimental results show that under various test conditions the DVV-MFPCC does better in its salient current tracking performances.

**Author Contributions:** The work presented here was carried out through the joint efforts of all authors, including concept proposal, paper work, and conducting experiments. Under C.-K.L.'s advice, H.-Q.H. and J.-T.W. are responsible for producing the experimental results and charting. C.-K.L. and J.-t.Y. are responsible for manuscript writing. H.-C.Y. and Y.-S.L. provided financial support and valuable suggestions for this work together with their participation of technical meetings. All authors have read and approved the form of current manuscript.

**Funding:** This research was funded by the Ministry of Science and Technology, Taiwan under grant numbers MOST 106-2221-E-019-053, 106-2221-E-019-070, 106-2218-E-033-008, and by National Taiwan Ocean University and National Taipei University of Technology under grant number USTP-NTUT-NTOU-107-01.

**Acknowledgments:** This manuscript is a result of joint research sponsored by the Ministry of Science and Technology of Taiwan, National Taiwan Ocean University, Chung Yuan Christian University, and National Taipei University of Technology under grant numbers MOST 106-2221-E-019-053, 106-2221-E-019-070, 106-2218-E-033-008 and USTP-NTUT-NTOU-107-01. The authors thank these institutions for their support.

**Conflicts of Interest:** The authors declare no conflict of interest.

## References

1. Sen, P.C. Electric motor drives and control-past, present, and future. *IEEE Trans. Ind. Appl.* **1990**, *37*, 562–575. [[CrossRef](#)]
2. Brod, D.M.; Novotny, D.W. Current control of VSI-PWM inverters. *IEEE Trans. Ind. Appl.* **1985**, *IA-21*, 562–570.
3. Kazmierkowski, M.; Krishnan, R.; Blaabjerg, F. *Control in Power Electronics*, 1st ed.; Academic Press: Cambridge, MA, USA, 2002.
4. Li, X.; Dusmez, S.; Akin, B.; Rajashekara, K. A new SVPWM for the phase current reconstruction of three-phase three-level T-type converters. *IEEE Trans. Power Electron.* **2016**, *31*, 2627–2637. [[CrossRef](#)]
5. Young, H.A.; Perez, M.A.; Rodríguez, J.; Abu-Rub, H. Assessing finite-control-set model predictive control: A comparison with a linear current controller in two-level voltage source inverters. *IEEE Ind. Electron. Mag.* **2014**, *8*, 44–52. [[CrossRef](#)]
6. Rodríguez, J.; Pontt, J.; Silva, C.A.; Correa, P.; Lezana, P.; Cortes, P.; Ammann, U. Predictive current control of a voltage source inverter. *IEEE Trans. Ind. Electron.* **2007**, *54*, 495–503. [[CrossRef](#)]
7. Hu, J.; Cheng, K.W.E. Predictive control of power electronics converters in renewable energy systems. *Energies* **2017**, *10*, 515. [[CrossRef](#)]
8. Nguyen, T.H.; Kim, K.-H. Finite control set-model predictive control with modulation to mitigate harmonic component in output current for a grid-connected inverter under distorted grid conditions. *Energies* **2017**, *10*, 907. [[CrossRef](#)]
9. Yang, X.; Liu, G.; Li, A.; Le, V.D. A predictive power control strategy for DFIGs based on a wind energy converter system. *Energies* **2017**, *10*, 1098. [[CrossRef](#)]
10. Jin, N.; Guo, L.; Yao, G. Model predictive direct power control for nonredundant fault tolerant grid-connected bidirectional voltage source converter. *Energies* **2017**, *10*, 1133. [[CrossRef](#)]
11. Guzmán, R.; de Vicuña, L.G.; Castilla, M.; Miret, J.; Camacho, A. Finite control set model predictive control for a three-phase shunt active power filter with a Kalman filter-based estimation. *Energies* **2017**, *10*, 1553. [[CrossRef](#)]
12. Chan, R.; Kwak, S. Model-based predictive current control method with constant switching frequency for single-phase voltage source inverters. *Energies* **2017**, *10*, 1927. [[CrossRef](#)]
13. Su, D.; Zhang, C.; Dong, Y. An improved continuous-time model predictive control of permanent magnetic synchronous motors for a wide-speed range. *Energies* **2017**, *10*, 2051. [[CrossRef](#)]

14. Dadu, A.M.; Mekhilef, S.; Soon, T.K.; Seyedmahmoudian, M.; Horan, B. Near state vector selection-based model predictive control with common mode voltage mitigation for a three-phase four-leg inverter. *Energies* **2017**, *10*, 2129. [[CrossRef](#)]
15. Wang, F.; Zhang, Z.; Mei, X.; Rodríguez, J.; Kennel, R. Advanced control strategies of induction machine: Field oriented control, direct torque control and model predictive control. *Energies* **2018**, *11*, 120. [[CrossRef](#)]
16. Chan, R.; Kwak, S. Improved finite-control-set model predictive control for cascaded H-bridge inverters. *Energies* **2018**, *11*, 355. [[CrossRef](#)]
17. Singh, V.K.; Tripathi, R.N.; Hanamoto, T. HIL co-simulation of finite set-model predictive control using FPGA for a three-phase VSI system. *Energies* **2018**, *11*, 909. [[CrossRef](#)]
18. Espi, J.M.; Castello, J. Capacitive emulation using predictive current control in LCL-filtered grid-connected converters to mitigate grid current distortion. *Energies* **2018**, *11*, 1421. [[CrossRef](#)]
19. Lin, C.-K.; Fu, L.-C.; Liu, T.-H.; Hsiao, C.-F. Passivity-based adaptive complementary PI sliding-mode speed controller for synchronous reluctance motor using predictive current control. In Proceedings of the 2012 American Control Conference (ACC 2012), Montreal, QC, Canada, 27–29 June 2012; pp. 1168–1173.
20. Lin, C.-K.; Liu, T.-H.; Yu, J.; Fu, L.-C.; Hsiao, C.-F. Model-free predictive current control for interior permanent-magnet synchronous motor drives based on current difference detection technique. *IEEE Trans. Ind. Electron.* **2014**, *61*, 667–681. [[CrossRef](#)]
21. Lin, C.-K.; Yu, J.-T.; Lai, Y.-S.; Yu, H.-C.; Lin, Y.-H.; Chen, F.-M. Simplified model-free predictive current control for interior permanent magnet synchronous motors. *IET Electron. Lett.* **2016**, *52*, 49–50. [[CrossRef](#)]
22. Lin, C.-K.; Yu, J.-T.; Lai, Y.-S.; Yu, H.-C. Improved model-free predictive current control for synchronous reluctance motor drives. *IEEE Trans. Ind. Electron.* **2016**, *63*, 3942–3953. [[CrossRef](#)]
23. Lin, C.-K.; Yu, J.-T.; Lai, Y.-S.; Yu, H.-C.; Hu, J.-W.; Wu, D.-Y. Two-vectors-based model-free predictive current control of a voltage source inverter. In Proceedings of the Advanced Mechanical Science and Technology for the Industrial Revolution 4.0, Fuzhou, China, 1–3 December 2016; pp. 227–233.
24. Wang, Y.; Wang, X.; Xie, W.; Wang, F.; Dou, M.; Kennel, R.M.; Lorenz, R.D.; Gerling, D. Deadbeat model-predictive torque control with discrete space-vector modulation for PMSM drives. *IEEE Trans. Ind. Electron.* **2017**, *64*, 3537–3547. [[CrossRef](#)]
25. Amiri, M.; Milimonfared, J.; Khaburi, A. Predictive torque control implementation for induction motors based on discrete space vector modulation. *IEEE Trans. Ind. Electron.* **2018**, *65*, 6881–6889. [[CrossRef](#)]



© 2018 by the authors. Licensee MDPI, Basel, Switzerland. This article is an open access article distributed under the terms and conditions of the Creative Commons Attribution (CC BY) license (<http://creativecommons.org/licenses/by/4.0/>).